

## Article

# Fault Diagnosis of PMSM Stator Winding Based on Continuous Wavelet Transform Analysis of Stator Phase Current Signal and Selected Artificial Intelligence Techniques

Przemyslaw Pietrzak  and Marcin Wolkiewicz \* 

Department of Electrical Machines, Drives and Measurements, Wrocław University of Science and Technology, Wybrzeże Wyspińskiego 27, 50-370 Wrocław, Poland

\* Correspondence: marcin.wolkiewicz@pwr.edu.pl

**Abstract:** High efficiency, high reliability and excellent dynamic performance have been key aspects considered in recent years when selecting motors for modern drive systems. These features characterize permanent magnet synchronous motors (PMSMs). This paper presents the application of continuous wavelet transform (CWT) and artificial intelligence (AI) techniques to the detection and classification of PMSM stator winding faults. The complex generalized Morse wavelet used for CWT analysis of three different diagnostic signals—the stator phase current, its envelope and the space vector module—is used to extract the symptoms most sensitive to the interturn short circuits (ITSCs) at the incipient stage of the damage. The effectiveness of automatic stator winding fault classification is compared for three selected ML algorithms: multilayer perceptron, support vector machine and k-nearest neighbors. The effect of the ML models' hyperparameters on their accuracy is also verified. The high effectiveness of the proposed methodology is confirmed by the results of the experimental verification carried out for different load torque levels and supply voltage frequency values.

**Keywords:** permanent magnet synchronous motor; fault diagnosis; condition monitoring; interturn short circuits; artificial intelligence; machine learning; continuous wavelet transform



**Citation:** Pietrzak, P.; Wolkiewicz, M. Fault Diagnosis of PMSM Stator Winding Based on Continuous Wavelet Transform Analysis of Stator Phase Current Signal and Selected Artificial Intelligence Techniques. *Electronics* **2023**, *12*, 1543. <https://doi.org/10.3390/electronics12071543>

Academic Editors: Ryad Zemouri, Mélanie Lévesque and Arezki Merkhouf

Received: 28 February 2023

Revised: 21 March 2023

Accepted: 22 March 2023

Published: 24 March 2023



**Copyright:** © 2023 by the authors. Licensee MDPI, Basel, Switzerland. This article is an open access article distributed under the terms and conditions of the Creative Commons Attribution (CC BY) license (<https://creativecommons.org/licenses/by/4.0/>).

## 1. Introduction

Over the past few decades, permanent magnet synchronous motors (PMSMs) have been widely used in various fields due to their high efficiency, high power density and good dynamic properties [1,2]. In recent years, when selecting motors for modern drive systems, special attention has also been paid to their power consumption and high durability. The properties of PMSM-based drives allow the requirements for using highly reliable and energy-saving solutions to be met [3]. Nevertheless, like any type of motor, PMSMs are prone to faults due to manufacturing defects, poor thermal management, overload operation, harsh environments and other internal and external factors.

Many faults have been analyzed and studied for PMSM drives, including mechanical (bearings, eccentricity, misalignment) [4], magnetic (demagnetization) [5], sensing (current, voltage, position) [6] and electrical (stator windings) [7,8] faults. Each of these faults is associated with negative effects on the operation of the drive system. Electrical faults related to the stator winding are among the most common and dangerous [9]. They are mainly short circuits caused by insulation damage. There are many possible sources of this damage, such as aging, overheating of the winding due to excessive electrical or mechanical stress, harsh environment and severe flux weakening.

A stator winding fault usually begins with a difficult-to-detect interturn short circuit (ITSC) in adjacent turns of the winding, and it can then lead very quickly to a more severe phase-to-phase or phase-to-ground short circuit. In the early stage of this failure, the motor may continue to operate because the ITSCs cause too little change in the amplitude of the stator phase currents, but heating in the shorted circuit can cause demagnetization of the

permanent magnet or complete damage to the motor. The motor's stator winding can be replaced if the short circuit is detected at an early stage. However, core damage caused by ground current flow is irreversible and may require the motor to be taken out of service [10]. For this reason, the greatest attention should be paid to detecting this type of damage at an incipient stage.

Fault diagnosis systems are increasingly used in industry. They are applied to monitor the condition of various types of machinery, especially electric motors. The development of an effective real-time diagnostic system makes it possible to detect various types of failures early, as soon as the first symptoms appear, rather than only at the critical stage of damage, and also to plan maintenance work in advance. This increases safety and reduces the repair and unplanned downtime costs [11]. However, there are challenges associated with the development of such systems. The first is related to the selection of the diagnostic signal, which carries information about the state of the motor. In the field of fault diagnosis, the aim is to use signals whose measurement is non-invasive, and which make it possible to extract symptoms that are highly sensitive to damage and insensitive to motor operating conditions changes, using signal processing methods. The choice of signal processing method is the second challenge. The application of the appropriate method allows the extraction of fault indicators whose increase may be indicative of a given damage. The third challenge for the development of modern fault diagnosis systems is to automate the detection process. In recent years, artificial intelligence (AI) techniques are increasingly being used to meet this requirement.

Currently, the stator phase current is the most commonly used diagnostic signal applied to detect electrical faults in AC motors. However, the stator winding fault can also affect other diagnostic signals. One of these signals is the voltage, including the stator phase voltage [12], the reference voltage in  $d$ - $q$  frame [13] and the stator voltage zero sequence component [14,15]. Symptoms of the stator winding fault can be also found in magnetic flux [16,17], back electromotive force [18], temperature, active power [10], vibration [19] and internal signals of the PMSM control structure [20,21]. Techniques based on parameter estimation are also popular in this field [22]. Nevertheless, the measurement of stator phase current signal is non-invasive and easy to implement. This signal also carries valuable information about the condition of the motor, which makes it the most attractive in the field of fault diagnosis [23].

In the literature, many signal processing methods have been proposed to extract stator winding fault symptoms from the stator phase current signal [24]. The most popular is the frequency domain analysis method based on fast Fourier transform (FFT): motor current signature analysis (MCSA) [25] and also extended park vector analysis (EPVA) based on spectral analysis of the module of the spatial current vector [26]. Among the method for performing frequency domain analysis are also high order transforms (HOTs). HOTs are based on high-order statistics and have also found applications in the fault diagnosis field. Particularly popular HOTs are bispectrum, estimation of signal parameter by rotational invariance (ESPRIT) and multiple signal classification (MUSIC) [27,28]. However, when using frequency domain analysis methods, information about the time of occurrence of a given component is lost, which is a significant drawback. Time–frequency domain analysis is devoid of these limitations.

Time–frequency domain analysis methods are very helpful in determining the time when the first symptoms of a given fault appear. This can make it possible at a later stage to determine the potential cause of the failure. The group of these methods includes Hilbert–Huang transform [29], Wigner–Ville distribution [30], short-time Fourier transform (STFT) [31] and continuous wavelet transform (CWT) [32]. In the fault diagnosis field, the effectiveness of the CWT analysis has been studied mainly for induction motors [33]. Nevertheless, despite its many advantages, it has not been studied in the past in terms of its applicability for extraction of the electrical faults of PMSMs at an incipient stage of failure. For this reason, the verification of the feasibility of applying this signal preprocessing

method to the extraction of the symptoms of ITSCs in the PMSM stator winding is in the scope of this paper.

The symptoms extracted using the above-mentioned signal processing methods can be used to train AI-based fault classifier models. In recent years, this is the most popular approach to automating the process of condition monitoring of electric motors. In the field of fault diagnosis, artificial neural networks (ANNs) are commonly used. Neural networks (NNs) with shallow structures, such as multilayer perceptron (MLP) [34], self-organizing Kohonen maps (SOMs) [35] and radial basis function (RBF) neural networks [4], have been particularly popular. Nonetheless, over the past few years, deep neural networks, such as long short-term memory (LSTM) and convolutional neural networks (CNNs), including those trained according to the transfer learning techniques, have become frequently used for such applications [28,32,36–40]. However, it should be emphasized that with the use of an appropriate diagnostic signal, as well as pre-processing method, it may be sufficient to apply a simple and easy-to-implement machine learning (ML) algorithm, such as k-nearest neighbors (KNN) or support vector machine (SVM) [41].

The first goal of this paper is to show and compare the possibility of extracting ITSC symptoms in the PMSM stator winding based on information obtained from complex generalized Morse wavelet-based CWT analysis of the stator current-based diagnostic signals: the stator phase current, its envelope and the space vector module. A direct comparison of the possibilities of extracting the symptoms of this type of PMSM fault from these three diagnostic signals using CWT, over a wide range of drive system operating conditions and fault severity, has not yet been presented in the literature, to the best of the authors' knowledge.

The second goal is to present a methodology for the automatic classification of PMSM stator winding faults using selected ML algorithms. A comparative study of three different ML algorithms, namely MLP, SVM and KNN, is carried out, including an analysis of the effect of ML model parameters on the effectiveness of the developed classifiers. Such analysis is often overlooked, but it can be very helpful in the process of preparing a diagnosis system. The main contributions of this study can be summarized as follows:

- Analysis of the effect of the ITSCs in PMSM stator winding on the waveforms of stator phase current, stator phase current envelope and stator phase current space vector module signal.
- Analysis of the possibility of extracting the symptoms of ITSCs in the PMSM stator winding from the stator phase current-based diagnostic signals using complex generalized Morse wavelet-based CWT analysis, and selection of the fault features that are most sensitive to this fault at the incipient stage.
- Development, experimental verification, hyperparameter tuning and comprehensive comparison of the effectiveness of three ML-based PMSM stator winding fault classifier models: MLP, SVM and KNN.
- Development of a methodology for automatic stator winding condition classification, operating on-line and providing the ability to detect and classify ITSCs.

The rest of the article is organized as follows: Section 2 describes the effect of PMSM stator winding faults on diagnostic signals that are based on stator phase current. Sections 3 and 4, respectively, present the theoretical foundations of the CWT and selected ML-based algorithms. In Section 5, the experimental setup is discussed. In Section 6, the results of the experimental verification, including the fault symptom extraction stage, as well as training, testing and comparison of the developed fault classifiers, are shown. Finally, Section 7 concludes the paper.

## **2. Analysis of the Effect of PMSM Stator Winding Fault on Diagnostic Signals Based on Stator Phase Current**

The theoretical analysis, including analytical models of a PMSM with ITSC faults, has been presented many times in the past in the literature [21,42]. This study focuses on the experimental study. The occurrence of an ITSC in the stator winding causes a current of

very high amplitude to flow in the shorted circuit. Nevertheless, the changes in stator phase current amplitude are not that significant and easy to recognize. The effect of the ITSCs in phase A of the PMSM stator winding on the stator phase current waveform for the rated frequency of power supply  $f_s = f_{sN} = 100$  Hz, different load torque  $T_L$  levels and number of shorted turns  $N_{sh}$  is shown in Figure 1. For each of the  $T_L$  set, in the range  $(0-1)T_N$ , a momentary ITSC of successively one to five turns in phase A of the PMSM stator winding is realized. Based on these waveforms it can be concluded that the ITSC causes an increase in the amplitude of the phase currents, and also their fluctuations. The largest increase is seen for the phase in which the short circuit occurred, i.e., phase A. Nevertheless, at the early stage of damage, especially with only one shorted turn ( $N_{sh} = 1$ ), the increase is much smaller. In addition, as is known, the amplitude of the current increases with increasing load torque.

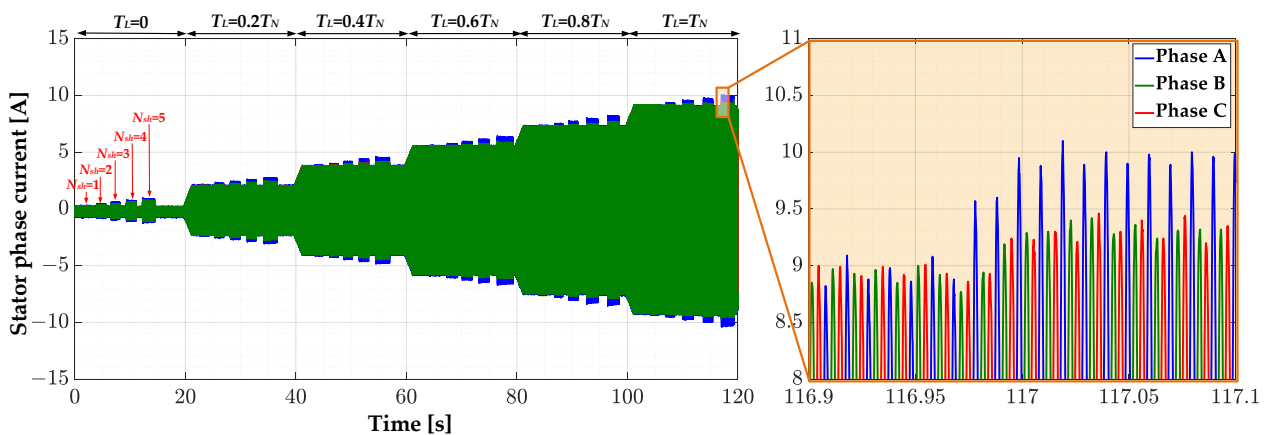


**Figure 1.** Effect of ITSCs in the PMSM stator winding on the waveforms of the stator phase currents, experimental study ( $T_L = \text{var}, f_s = f_{sN} = 100$  Hz).

Fluctuations in the amplitude of the stator phase current can be isolated by calculating the envelope of this signal. Hilbert transform (HT) can be used to determine the envelope, according to the following equation [23]:

$$i_s^H(t) = \sqrt{i_s^2(t) + H^2[i_s(t)]}, \tag{1}$$

where  $H[i_s(t)]$  is the HT of the stator phase current calculated [43]:

$$H[i_s(t)] = \frac{1}{\pi} \int_{-\infty}^{+\infty} \frac{i_s(\tau)}{t - \tau} d\tau. \tag{2}$$

The effect of the ITSCs in the PMSM stator winding for the same operating and winding conditions is presented in Figure 1, and the effect on the stator phase current envelope of the damaged phase (phase A) is shown in Figure 2. The value of the envelope increases as a result of the ITSCs, and greater the degree of fault ( $N_{sh}$ ), the greater the increase. As with the stator current signal, the amplitude of the envelope also significantly depends on the  $T_L$  value.

Symptoms of the stator winding faults can be sought also in the stator phase current space vector module [23,44]. It is based on the root of the sum of the squares of the stator phase current components in the  $\alpha$ - $\beta$  reference frame, calculated according to the following equation:

$$|i_s| = \sqrt{i_{s\alpha}^2 + i_{s\beta}^2}, \tag{3}$$

where  $i_{s\alpha}$  and  $i_{s\beta}$  are determined as follows:

$$\begin{aligned} i_{s\alpha} &= \sqrt{\frac{2}{3}} \cdot \left( i_{sA} - \frac{1}{2} \cdot (i_{sB} + i_{sC}) \right), \\ i_{s\beta} &= \frac{1}{\sqrt{2}} (i_{sB} - i_{sC}) \end{aligned} \tag{4}$$

and  $i_{sA}$ ,  $i_{sB}$  and  $i_{sC}$  are stator currents in phases A, B and C, respectively.

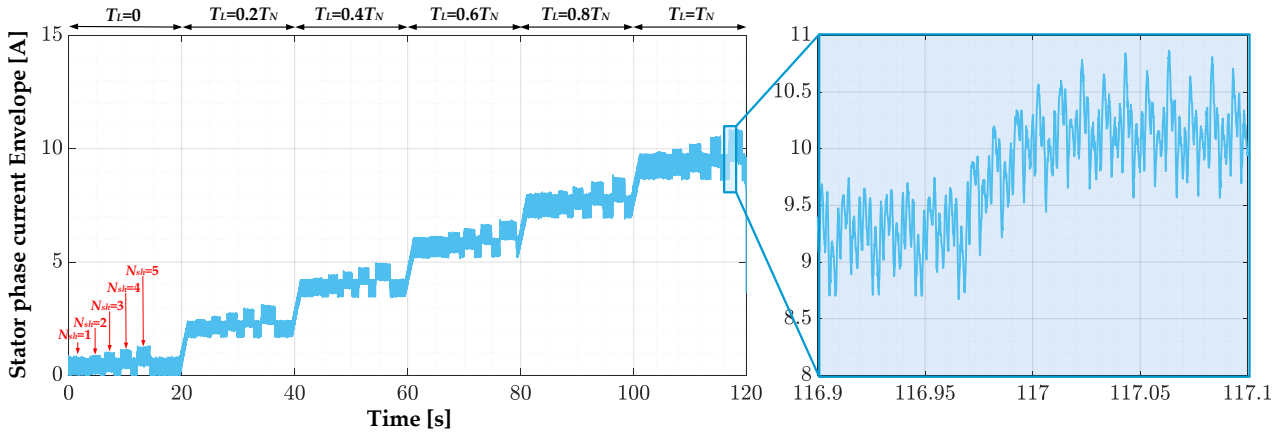


**Figure 2.** Effect of ITSCs in the PMSM stator winding on the waveform of the stator phase current envelope (phase A), experimental study ( $T_L = \text{var}$ ,  $f_s = f_{sN} = 100$  Hz).

The effect of the ITSCs on the stator currents space vector module waveform is presented in Figure 3. Both ITSCs and load torque affect it in a way similar to that seen for the stator phase current envelope. Therefore, to isolate only the symptoms of the stator winding fault, the diagnostic signals discussed above will be processed using CWT analysis.

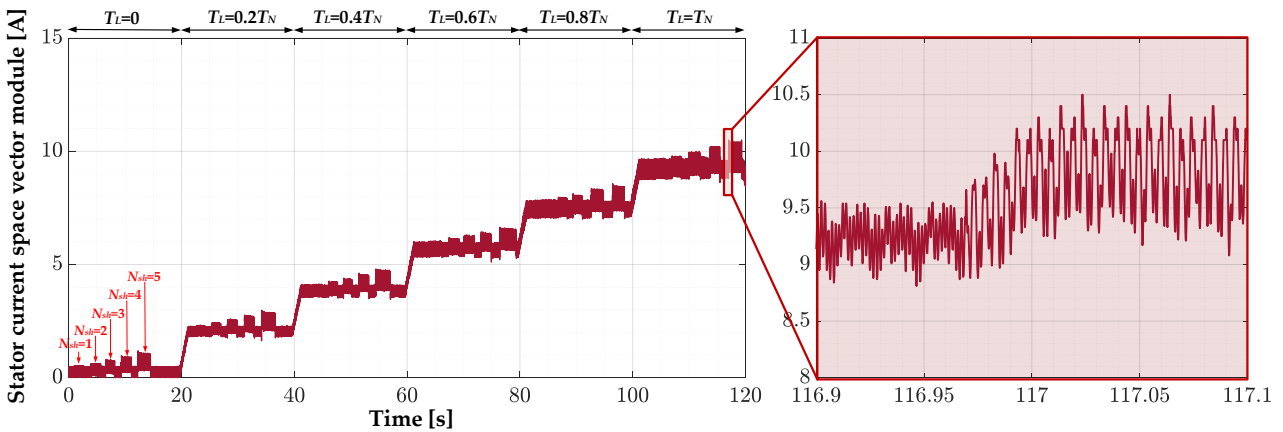


**Figure 3.** Effect of ITSCs in the PMSM stator winding on the waveform of the stator phase current space vector module, experimental study ( $T_L = \text{var}$ ,  $f_s = f_{sN} = 100$  Hz).

### 3. Continuous Wavelet Transform Theoretical Basis

Methods that perform time–frequency analysis are used to describe the relationship between signal information in the time domain and its spectral distribution in the frequency domain [45]. This group of methods is particularly useful in the process of extracting symptoms of electric motor failures. CWT is one of the methods belonging to this group. The result of CWT contains both time and frequency information of the analyzed signal [46]. CWT has found application in the field of fault diagnosis in the past, but mainly for

the extraction of mechanical damages of induction motors [33,47,48]. CWT of a square-integrable signal  $x(t)$  is calculated as follows [47]:

$$CWT(\tau, a) = \int x(t) \psi_{a,\tau}^*(t) dt = \frac{1}{\sqrt{|a|}} \int x(t) \psi^*\left(\frac{t-\tau}{a}\right) dt, \quad (5)$$

where  $a$  is the scale factor and  $\tau$  denotes the shift parameter,  $\psi$  is a mother wavelet,  $\psi^*(\cdot)$  represents the complex conjugate of function  $\psi(\cdot)$  and  $\psi_{a,\tau}$  is called a baby wavelet and is translated and scaled version of a mother wavelet [46]:

$$\psi_{a,\tau} = \frac{1}{\sqrt{|a|}} \psi\left(\frac{t-\tau}{a}\right). \quad (6)$$

The integral in Equation (6) is replaced by the summation in the digital implementation of CWT [49]:

$$CWT(n, a) = \frac{1}{\sqrt{|a|}} \sum x(t) \psi^*\left(\frac{k-n}{a}\right). \quad (7)$$

A mother wavelet function can be any function that meets kernel conditions. Different types of wavelets can be found in the literature, such as Daubechies wavelets [50], bump wavelets, complex generalized Morse wavelets or complex Morlet wavelets [51].

The time and frequency resolution of CWT analysis vary with the scale factor  $a$ . Scale is proportional to the inverse of the frequency [52]. In the scope of our article, the focus is on the verification of the possibility of using CWT analysis to extract symptoms of PMSM stator winding faults, so a detailed description of the theory behind CWT is omitted, but it can be found in [51,53,54].

#### 4. Machine Learning-Based Algorithms

In the process of automatic fault classification, the effectiveness of three selected AI-based techniques—ML algorithms—is compared. The selection of an appropriate fault classifier model is extremely important, with the goal of maximizing its effectiveness. This section discusses the theoretical basis of the MLP, SVM and KNN algorithms.

##### 4.1. MLP

There are different types of NN structures described in the literature [55]. Nevertheless, one of the most popular that has found application in the field of electric motor fault diagnosis is the MLP. The construction of the MLP model typically consists of input layer, one or more hidden layers and an output layer [56]. It has been found that an MLP structure with only two hidden layers can estimate any continuous vector-valued function [57]. The simplified principle of data transfer in MLPs can be described in three main steps [58]:

1. Input signals are initially scaled using input weights  $w_{ij}$ .
2. Input signals of each hidden neuron are summed and recalculated using the activation function.
3. Output neuron is introduced to sum the signals scaled by the activation function, which come from the outputs of the hidden layers.

The output of the neuron, which is a function  $f$  of weighted inputs summed with the bias value, can be expressed as follows:

$$\text{out}_i = f\left(\sum_{j=1}^n w_{ij} x_j + b_i\right), \quad (8)$$

where  $x_j$  and  $b_i$  are weights and biases associated with neuron  $i$ .

The structure of the MLP network has a significant effect on the accuracy of the model. The output signal of the network with two hidden layers can be described by the following equation:

$$y_k = f^{(2)}\left(\sum_{m=1}^M w_{km}^{(2)} f^{(1)}\left(\sum_{n=1}^N w_{mn}^{(1)} x_n + w_{m0}^{(1)}\right) + w_{k0}^{(2)}\right), \quad (9)$$

where  $x_n$  is the  $n$ -th value of the input,  $y_k$  is the output value of the  $k$ -th neuron,  $f^{(1)}$  and  $f^{(2)}$  are the activation functions of the first and second layers and  $w$  is the weight of the neuron in the selected layer.

The MLP network acts as an approximator of the learning data. The training process of MLPs involves the use of input–output data in order to determine the weights and biases. The training function updates the weight and bias values to minimize the objective function, usually the mean square error (MSE) of the output value in relation to the actual value. There are different training methods for MLPs described in the literature. Nevertheless, one of the most popular and fastest MLP training algorithms is the Levenberg–Marquardt optimization [59,60].

#### 4.2. SVM

SVM is an ML algorithm utilized to solve classification problems; it was first proposed by Vladimir Vapnik [61]. It is based on the statistical learning theory and has found application in many fields, including text categorization and pattern recognition [41]. The main objective of the SVM is to find the hyperplane that separates data points that belong to one class from the points that belong to another class as much as possible, to maximize the margin. The data points that are closest to the hyperplane are called support vectors.

Depending on the classification problem under consideration, different kernel functions  $K$  are used. The use of a kernel function is called the kernel trick and is applied to make linear classification possible by mapping data from the original input space to a high-dimensional feature space [62]. Various types of kernel functions can be found in the literature. Nevertheless, the most common are the linear kernel function, polynomial kernel function and Gaussian kernel function (GKF). They are described by Equations (10)–(12). It has been proven that the GKF has a very good generalization ability for different types of datasets [62]. The more detailed mathematical foundations of this algorithm are discussed in [61–64].

$$K_{\text{Linear}}(x_1, x_2) = x_1^T x_2 \quad (10)$$

$$K_{\text{Polynomial}}(x_1, x_2) = (x_1^T x_2 + 1)^\gamma \quad (11)$$

$$K_{\text{Gaussian}}(x_1, x_2) = e^{-\left(\frac{\|x_1 - x_2\|^2}{2\sigma^2}\right)} \quad (12)$$

where  $\sigma$  is the width of the Gaussian function and  $\gamma$  is the polynomial degree.

#### 4.3. KNN

The last ML model under analysis is based on the simple KNN algorithm. The KNN algorithm is one of the most popular pattern recognition methods. It has found application in various classification problems. The basic concept of the KNN is that the actual labels of classes are known for the training dataset. Then, when the new data are processed, the KNN algorithm calculates the distance between the new point and points from the training dataset. The category of the new data is the category that appears the most frequently among the nearest  $K$  points, where  $K$  is a hyperparameter of the KNN model and is known as the nearest neighbor value. The choice of the  $K$  value has an impact on the determination of the categories of unknown points [65].

When determining whether a new point and known points from a training dataset belong to the same class, the distance between the nearest points is calculated. Various distance metrics for calculating the distance between these points are known in the literature. Assuming that  $A$  and  $B$  are feature vectors,  $A = (x_1, x_2, \dots, x_n)$  and  $B = (y_1, y_2, \dots, y_n)$ , where  $n$  is the dimensionality of the feature space. The most common distance metrics are Euclidean, Minkowski and correlation, which can be calculated as follows:

$$d_{\text{Euclidean}}(A, B) = \sqrt{\sum_{i=1}^n (x_i - y_i)^2} \quad (13)$$

$$d_{\text{Minkowski}}(A, B) = \left( \sum_{i=1}^n |x_i - y_i|^r \right)^{\frac{1}{r}} \quad (14)$$

$$d_{\text{Correlation}}(A, B) = \frac{\sum_{i=1}^n (x_i - \mu_i)(y_i - \mu_i)}{\sqrt{\sum_{i=1}^n (x_i - \mu_i)^2 \sum_{i=1}^n (y_i - \mu_i)^2}} \quad (15)$$

## 5. Experimental Setup

Experimental tests were conducted on a 2.5 kW PMSM produced by Lenze. The parameters of this motor are grouped in Table A1 in Appendix A. This motor was coupled to a PMSM with a nominal power of 4.7 kW, ensuring load torque. Both motors were powered from voltage source inverters (VSIs). The analyzed PMSM operated under field-oriented control (FOC). The inverter of the second PMSM operated in torque regulation mode. Stator phase current signals were measured with LA 25-NP current transducers by produced LEM. The data acquisition system was based on the eight-channel NI PXI-4492 DAQ card produced by National Instruments, which was inside an NI PXI 1082 industrial PC. The motor control was realized in Lenze Engineer environment, whereas load torque was set in Veristand. LabVIEW and MATLAB software were used to create a stator winding fault diagnosis system. The application responsible for data acquisition was developed in the LabVIEW environment. Figure 4a shows an illustrative block diagram of the experimental setup, while Figure 4b shows an actual view of the key components of this setup.

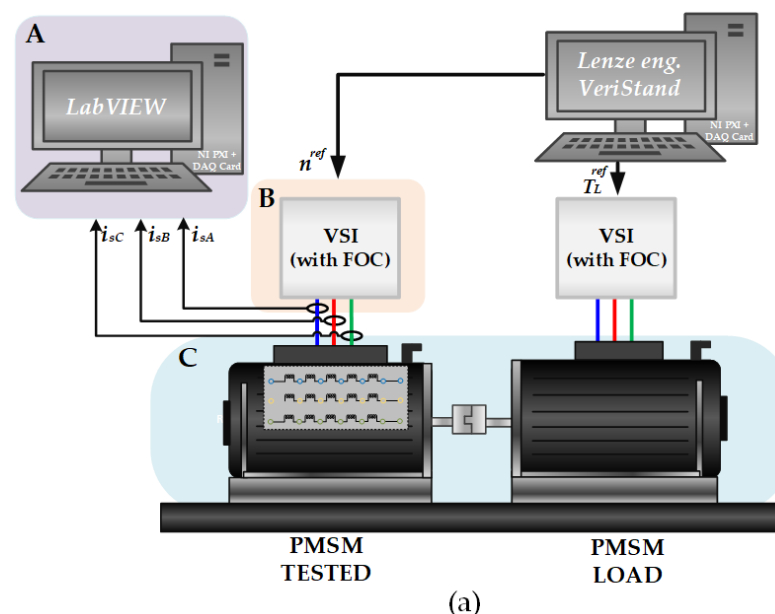
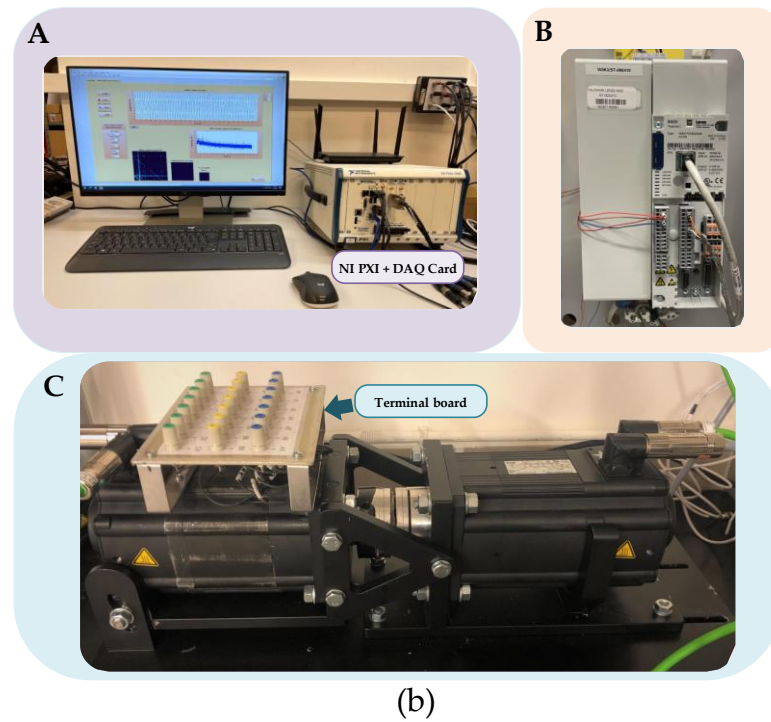
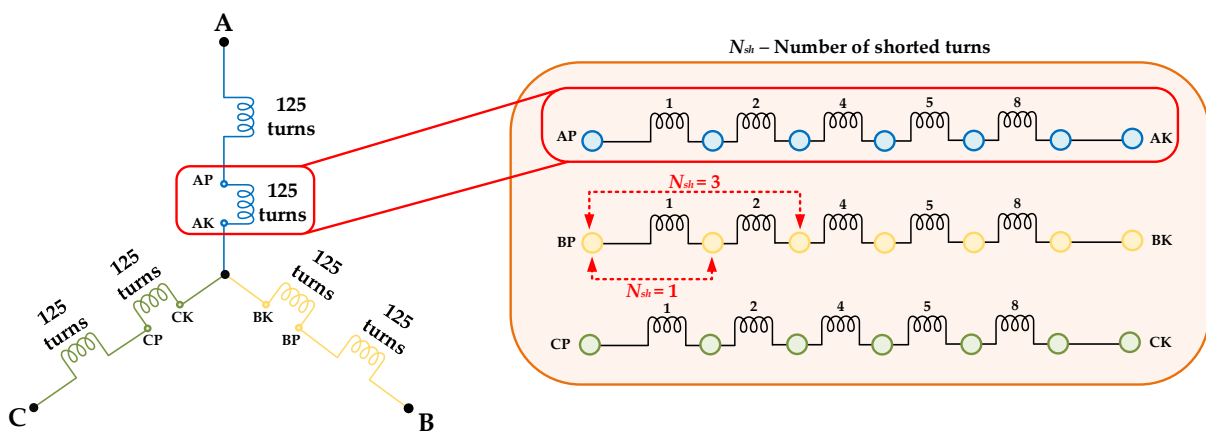


Figure 3. Cont.



**Figure 4.** Experimental setup: (a) illustrative block diagram; (b) real view. A—NI PXI with DAQ card, B—VSI by Lenze, C—motor test bench.

The stator winding construction of the PMSM under test was specially prepared to allow physical modeling of the ITSCs of several turns. In each of the phases, a group of coils was led out to the terminal board. This terminal board can be seen at the top of the motor in Figure 4b. The illustrative diagram of the PMSM stator windings and this board are shown in Figure 5. In order to physically model the ITSC fault, the taps that correspond to the selected number of turns  $N_{sh}$  were connected through a metallic connection with a wire. The examples of such connections for  $N_{sh} = 1$  and  $N_{sh} = 3$  are shown as red arrows in Figure 5.



**Figure 5.** Illustrative diagram of the PMSM stator windings and terminal board.

In the course of the experiments, the incipient stator winding faults (1–5 shorted turns) were analyzed. The minimum number of shorted turns ( $N_{sh} = 1$ ) represents 0.4% of all turns in a phase.

## 6. Results

The experimental verification carried out within the framework of this study is divided into a part related to the extraction of PMSM stator winding fault symptoms and a part devoted to the classification of winding conditions. All tests were performed on the already presented motor test bench. The results and their discussion are included in the following subsections.

### 6.1. CWT-Based PMSM Stator Winding Fault Symptom Extraction

The choice of a method for extracting fault symptoms is crucial in the development of condition monitoring and fault diagnosis systems. To this end, this research proposes a time–frequency domain analysis using CWT. CWT analysis makes it possible to determine not only the distribution of harmonics in the signal, the increase in which can indicate a motor fault, but also the timing of their occurrence. This may help determine the cause of the failure. The results presented in this section are obtained for the complex generalized Morse wavelet that is defined as follows [52–54]:

$$\psi_{\beta,\gamma}(\omega) = U(\omega)a_{\beta,\gamma}\omega^\beta e^{-\omega\gamma}, \quad (16)$$

where  $\alpha_{\beta,\gamma}$  is a normalization constant,  $U(\omega)$  is the unit step function, and  $\beta$  and  $\gamma$  are parameters that control the wavelet form. The normalization constant is calculated according to Equation (17) [52].

$$a_{\beta,\gamma} \equiv 2 \left( \frac{e\gamma}{\beta} \right)^{\frac{\beta}{\gamma}}. \quad (17)$$

In *MATLAB Wavelet Toolbox*, which is used in the scope of this work, the parameters of the generalized Morse wavelet are defined as  $\gamma$  and the time–bandwidth product  $P^2 = \beta\gamma$ , and they correspond directly to the analysis in [52–54]. The parameters of the Morse wavelet used are  $\gamma = 3$  and  $\beta = 20$ . An analysis of the effect of these values on the wavelet shape is presented in [54].

A comparative study of the possibility of extracting the symptoms of ITSCs using CWT of three diagnostic signals, namely the stator phase current, stator phase current envelope and stator phase current space vector module, which were characterized in Section 2, is carried out. The experimental verification was realized over a wide range of motor operating conditions and different severities of damage ( $N_{sh}$ ). The stator phase current scalogram for rated power supply frequency ( $f_s = f_{sN} = 100$  Hz), different  $T_L$  levels and cyclic momentary short-circuiting of one to five turns is shown in Figure 6a. On this scalogram, the dominant amplitude values of the CWT coefficients for the component corresponding to the frequency of the supply voltage ( $f_s$ ) are visible. The significant influence of the load torque level on the amplitudes of these components is visible—it increases as the load torque increases. Nevertheless, a slight increase in the value of the  $3f_s$  frequency component amplitude as a result of the stator winding fault is also visible. It is a typical symptom of the PMSM stator winding fault, which has been proven by the authors, among others, in [23]. Therefore, in order to analyze the part of the scalogram related to this component, omitting the fundamental frequency component, Figure 6b,c show 2D and 3D scalograms for the narrowed frequency (150–600 Hz) and a colormap (0–0.5 A) range. Due to the above narrowing of the frequency and colormap range, the increase in the values of the coefficients related to the  $3f_s$  component  $|CWT_{isA}(3f_s, t)|$  is better seen.

Figure 7 shows the raw and filtered (moving average filter with a window of 2048 samples that correspond to 0.25 s) waveforms of the  $|CWT_{isA}(3f_s, t)|$ , with the exact moments of short-circuit occurrence marked. The range of the vertical axis is adjusted to be the same as for the diagnostic signals that remain to be analyzed (stator phase current envelope and space vector module). Based on an analysis of this waveform, it is possible to determine a clear increase in the value of this component caused by the ITSCs. Nevertheless, these increases are practically invisible for the early stage of damage—for one shorted turn ( $N_{sh} = 1$ ). There is also a slight influence of the load torque level on these value changes.

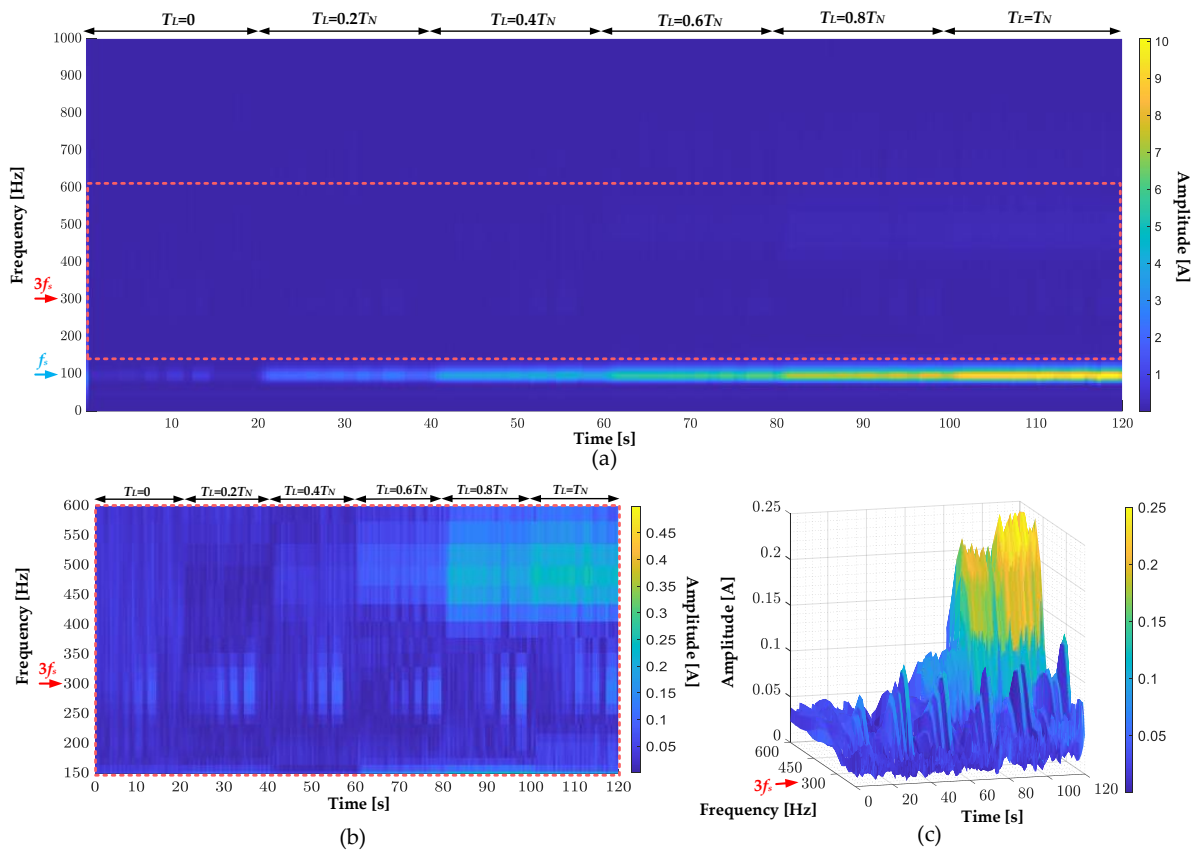


Figure 6. (a) CWT scalogram of the stator phase current waveform; (b) 2D and (c) 3D scalograms of the stator phase current waveform for narrowed frequency and colormap range ( $T_L = \text{var}$ ,  $f_s = f_{sN} = 100$  Hz).

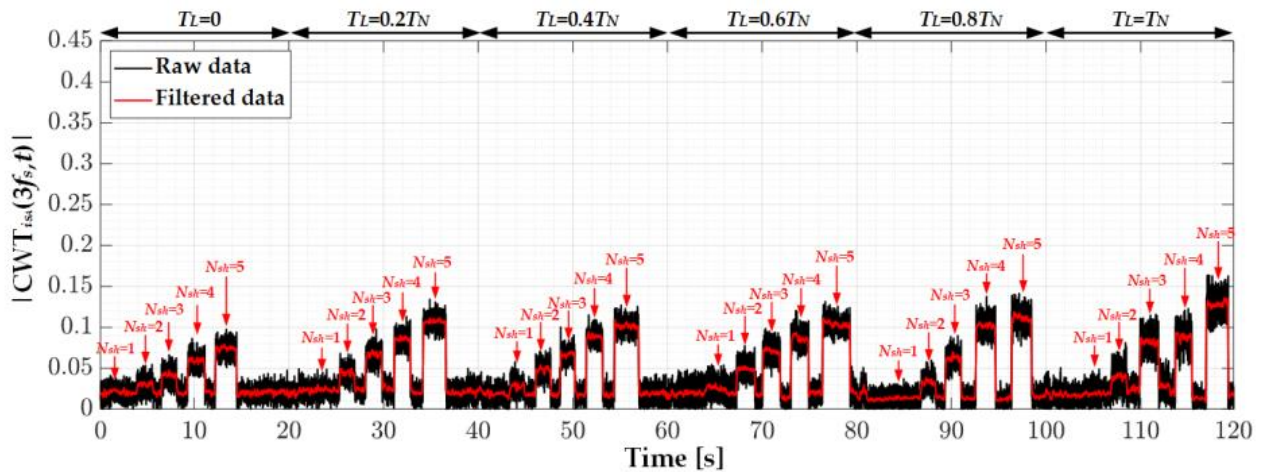
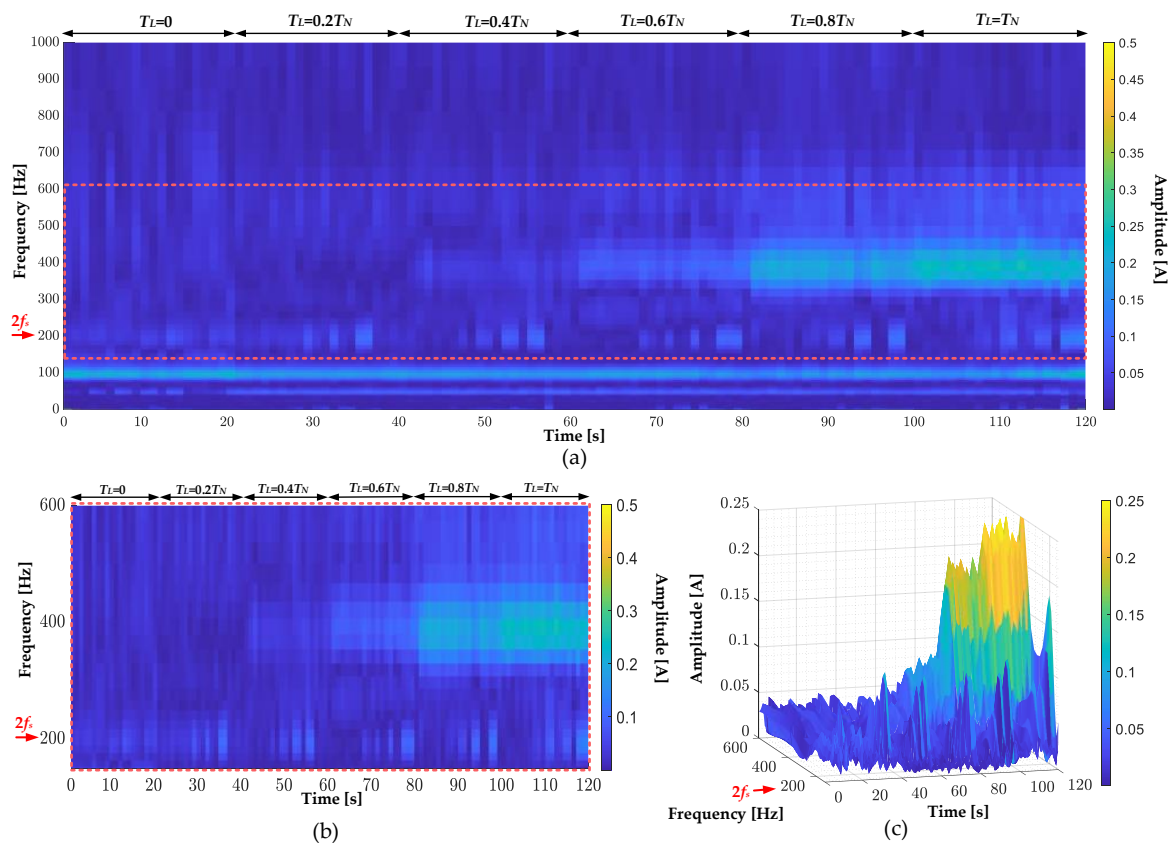


Figure 7. The raw and filtered waveforms of the  $|CWT_{isA}(3f_s, t)|$  value during the cyclic momentary short-circuiting of 1 to 5 turns and different load torque levels ( $T_L = \text{var}$ ,  $f_s = f_{sN} = 100$  Hz).

The presentation of the results of the CWT analysis, including the frequency and colormap range, for the remaining diagnostic signals will be retained. Figure 8 shows 2D and 3D scalograms of the stator phase current envelope signal. For this signal, the increase in the values of the CWT coefficients related to the second harmonic, the  $2f_s$  component  $|CWT_{is}^H A(2f_s, t)|$ , is visible.



**Figure 8.** (a) CWT scalogram of the stator phase current envelope waveform; (b) 2D and (c) 3D scalograms of the stator phase current envelope waveform for narrowed frequency range ( $T_L = \text{var}, f_s = 100$  Hz).

Figure 9 shows the raw and filtered waveforms of  $|CWT_{is}^H(2f_s, t)|$ . The increases in its value caused by the ITSC are very similar to those for the  $3f_s$  component for the stator phase current. Nevertheless, for the unloaded motor ( $T_L = 0$ ), the increase is less notable.

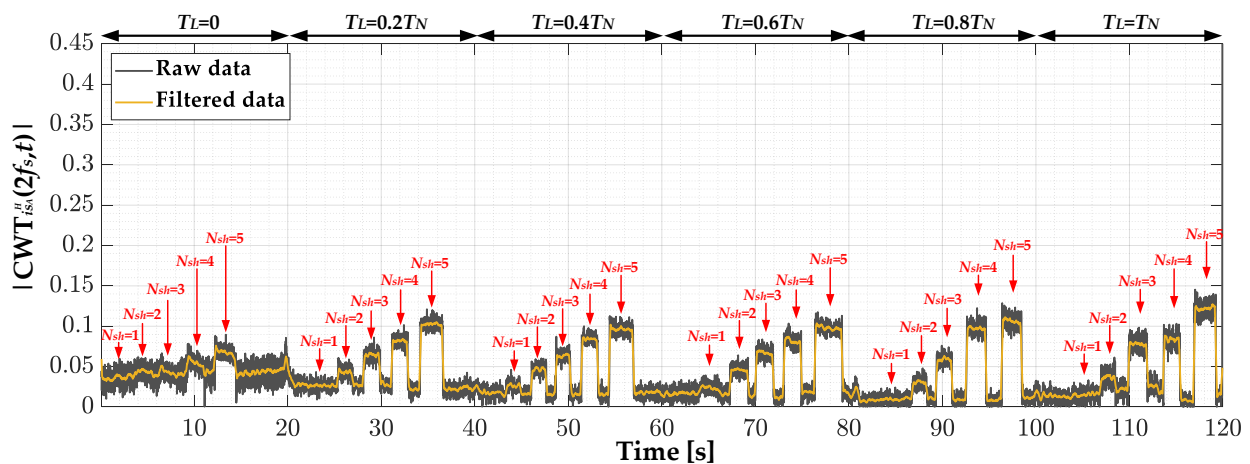


**Figure 9.** The raw and filtered waveforms of the  $|CWT_{is}^H(2f_s, t)|$  value during the cyclic momentary short-circuiting of 1 to 5 turns and different load torques levels ( $T_L = \text{var}, f_s = f_{sN} = 100$  Hz).

In Figure 10, the 2D and 3D CWT scalograms of the stator phase current space vector module signal are presented. In this case, as for stator phase current envelope CWT analysis, the increase in the value of the coefficient related to the second harmonic, the  $2f_s$  component  $|CWT_{is1}(2f_s, t)|$ , is visible. Figure 11 shows the raw and filtered waveforms

of its amplitude. The increases in the value caused by the ITSC are much more significant compared to the previously analyzed signals, also at the incipient stage of the failure—for  $N_{sh} = 1$ —in the whole range of the analyzed load torques.

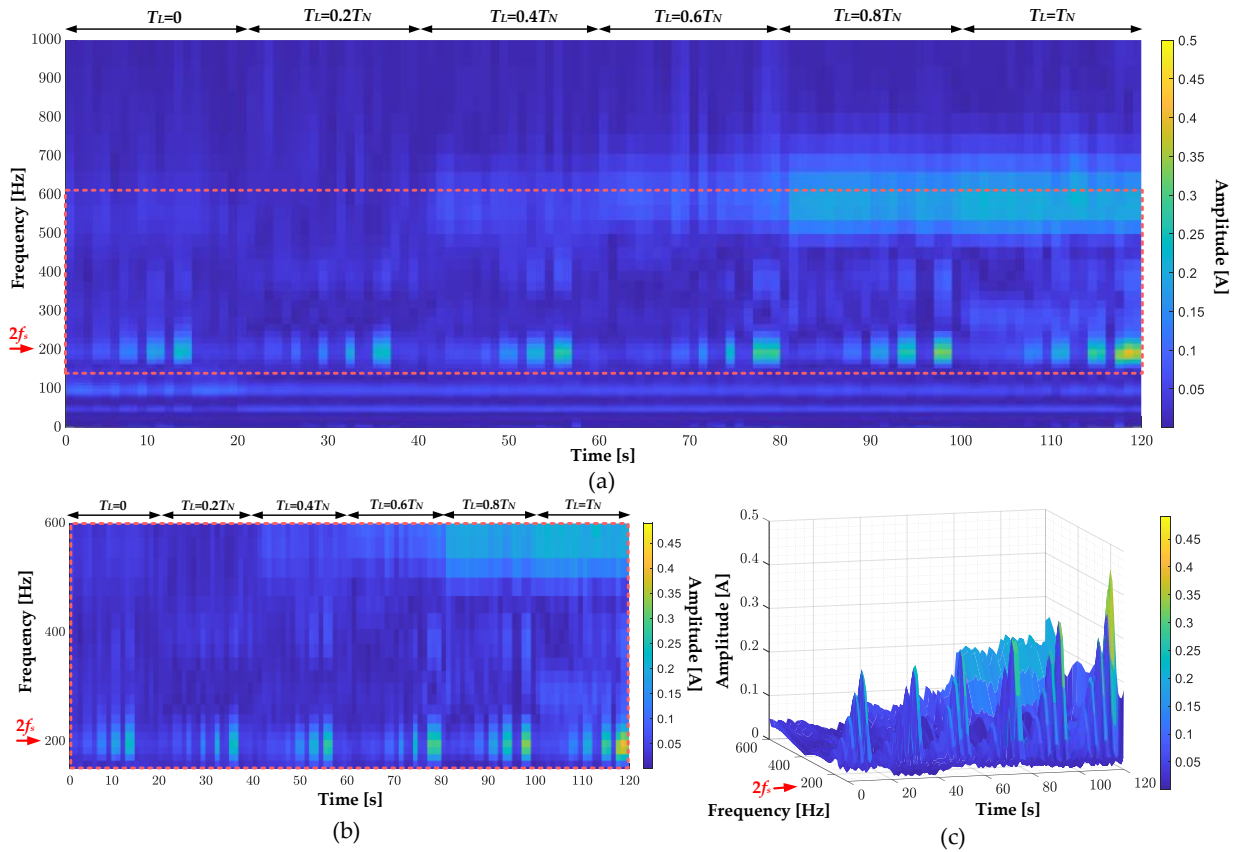


Figure 10. (a) CWT scalogram of the stator phase current space vector module waveform; (b) 2D and (c) 3D scalograms of the stator phase current envelope waveform for narrowed frequency and colormap range ( $T_L = \text{var}$ ,  $f_s = 100$  Hz).

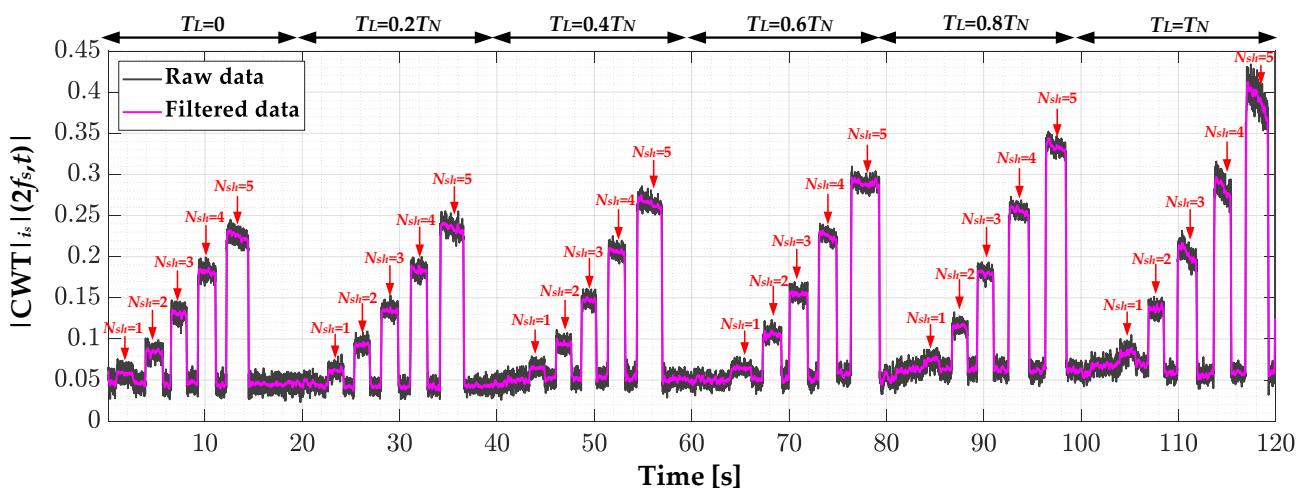
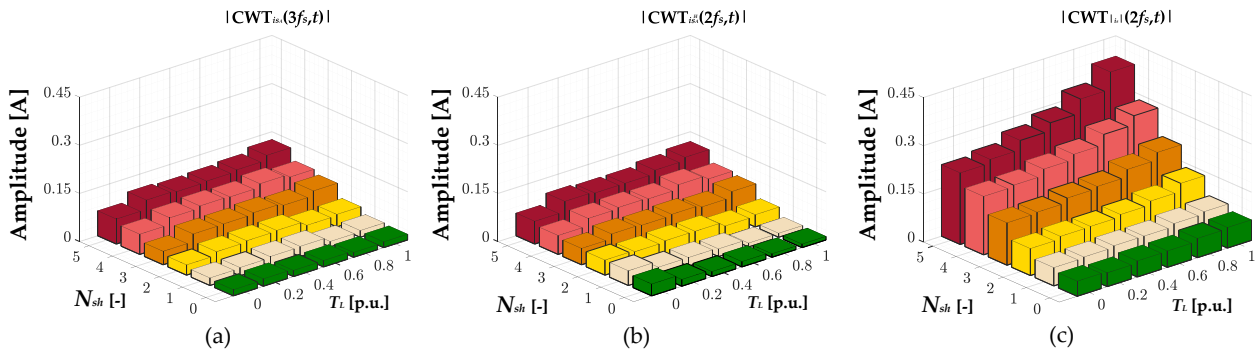


Figure 11. The raw and filtered waveforms of the  $|CWT|_{isA} |(2f_s, t)|$  value during the cyclic momentary short-circuiting of 1 to 5 turns and different load torque levels ( $T_L = \text{var}$ ,  $f_s = f_{sN} = 100$  Hz).

In order to make a final comparison of the sensitivity to stator winding fault of the extracted symptoms and to select those to be used as elements of the input vector of the ML models, Figure 12 shows the effect of  $T_L$  and  $N_{sh}$  on the value of their amplitudes.

Moreover, the effect of power supply frequency and  $N_{sh}$  is presented in Figure 13. The greatest sensitivity to the increasing severity of the stator winding fault ( $N_{sh}$ ), in the whole range of the analyzed motor operating conditions and also for the incipient stage of the failure, is achieved for the  $|CWT_{|is|}(2f_s, t)|$  value. It can also be seen that there is little effect of the load torque and the frequency of the supply voltage on these values. Based on the analysis of these results, it is decided to use the value of  $|CWT_{|isA|}(2f_s, t)|$  as one of the elements of the ML-based fault classifier model input vector. In the next section, the automation process of the PMSM stator winding fault classification will be presented.



**Figure 12.** The effect of  $N_{sh}$  in the PMSM stator winding and  $T_L$  level on the amplitude of the extracted symptoms (a)  $|CWT_{isA}(3f_s, t)|$ , (b)  $|CWT_{is}^H(2f_s, t)|$  and (c)  $|CWT_{|isA|}(2f_s, t)|$  ( $f_s = f_{sN} = 100$  Hz).

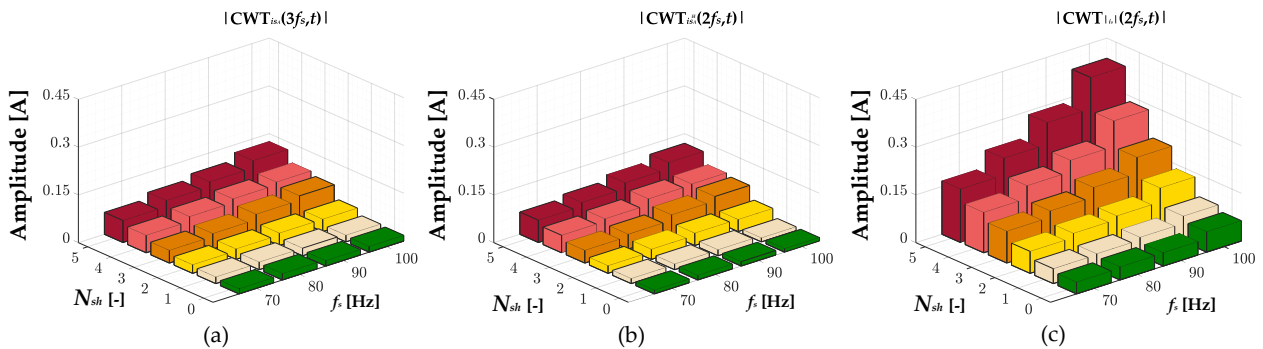


**Figure 13.** The effect of  $N_{sh}$  in the PMSM stator winding and  $f_s$  value on the amplitude of the extracted symptoms (a)  $|CWT_{isA}(3f_s, t)|$ , (b)  $|CWT_{is}^H(2f_s, t)|$  and (c)  $|CWT_{|isA|}(2f_s, t)|$  ( $T_L = T_N$ ).

### 6.2. ML-Based Classification of PMSM Stator Winding Condition

The application of ML algorithms with the carefully selected elements of the input vector can be useful in the process of automating fault diagnosis and condition monitoring. One of the elements of the input vector is the value of the  $|CWT_{|isA|}(2f_s, t)|$  which was proven to be very sensitive to the stator winding fault. In order to make the developed fault classifier models robust to the changes in the operating conditions of the drive system, the filtered value of  $|i_s|$ , which carries information about the load torque level  $T_L$ , as shown in Figure 2, and the value of the supply voltage frequency  $f_s$  are also used as vector elements. Therefore, the final form of the input vector is as follows:  $X = [|CWT_{|is|}(2f_s, t)|, |i_{s\text{filtered}}|, f_s]$ . The dataset specification is as follows: it consists of 5000 labeled vectors that correspond to the different conditions of the PMSM stator winding  $N_{sh} = \{0; 1; 2; 3; 4; 5\}$  and also different operating conditions:  $T_L = \{0; 0.2T_N; 0.4T_N; 0.6T_N; 0.8T_N; T_N\}$ ,  $f_s = \{80 \text{ Hz}; 90 \text{ Hz}; 100 \text{ Hz}\}$ . Seventy percent of all vectors (3500) are used for the training process, and the remaining 30% (1500) are used for off-line tests. This dataset was obtained through experimental research conducted on a specially prepared setup, which is described in Section 6.

### 6.2.1. MLP

MLP is the first of the PMSM stator winding fault classifier models analyzed. In the process of preparing the MLP model, the most important thing is the selection of the structure of the network. One of the most common approaches to solve this problem is the constructivist approach: starting with a very simple network structure, i.e., one hidden layer with a small number of neurons, and gradually adding neurons in this layer, and optionally more hidden layers, while verifying the accuracy of the model for each case. Model accuracy is calculated as the number of correctly classified winding conditions  $n_{correct}$  divided by the number of vectors contained in the training dataset  $N$ :

$$\text{Accuracy} = \frac{n_{correct}}{N} \cdot 100\%. \quad (18)$$

In the scope of this research, the training process of the MLP model is realized with the use of Levenberg–Marquardt gradient algorithm. The maximum number of epochs is set to 1000, and the hidden layer activation function is the hyperbolic tangent sigmoid transfer function. The MLP-based fault classifier model accuracies for different NN structures are grouped in Table 1. The values of the loss function (MSE) during the training process for each of the verified NNs are shown in Figure 14. The lowest accuracy (96.5%) is achieved for the MLP with the smallest number of neurons (seven) in the hidden layer—{3-7-1}. The highest accuracy of 98.1% is achieved by an MLP structure with one hidden layer with 21 neurons—{3-21-1}. The raw responses of the MLP classifier to the test vectors are shown in Figure 15, whereas the responses are rounded to the nearest integer value in Figure 16. In order to evaluate the overall effectiveness of the models developed, two metrics are introduced: classification effectiveness  $C_{EFF}$  and precision.

**Table 1.** MLP classifier accuracies for different structures of the network.

MLP Structure	Accuracy
{3-7-1}	96.5%
{3-9-1}	97.2%
{3-11-1}	97.4%
{3-13-1}	97.9%
{3-15-1}	97.8%
{3-17-1}	98.0%
{3-19-1}	98.0%
<b>{3-21-1}</b>	<b>98.1%</b>
{3-23-1}	96.7%

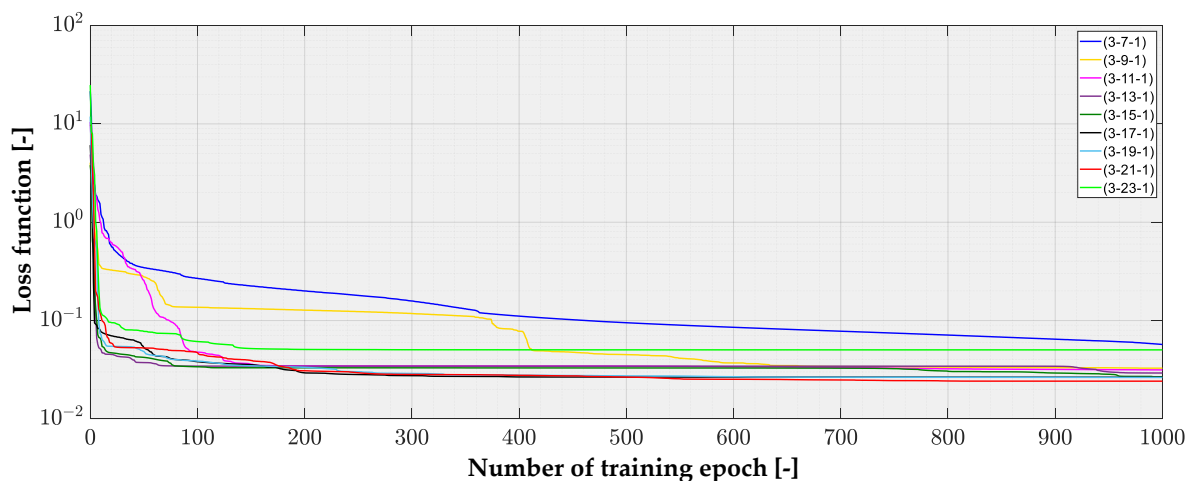


**Figure 14.** Loss (MSE) function during the training process of the MLP models with different structures.

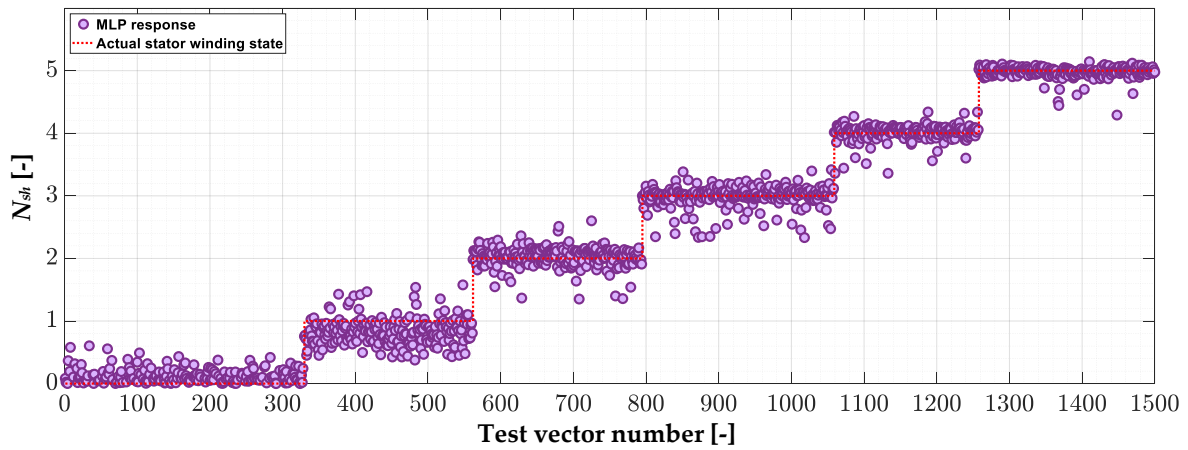


Figure 15. Raw responses of the MLP-based fault classifier model to the test vectors.

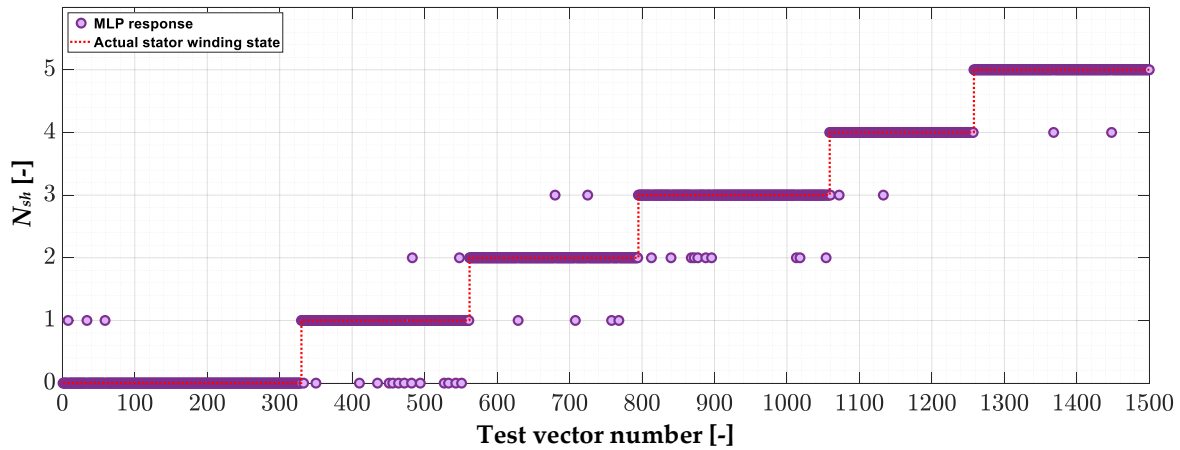


Figure 16. Rounded responses to the nearest integer of the MLP-based fault classifier model to the test vectors.

$C_{EFF}$  index determines the ratio of the correctly classified stator winding states  $Y_C$  to the number of input vectors  $Y_M$ —sum of the correct classifications and misclassifications:

$$C_{EFF} = \frac{Y_C}{Y_C + Y_M} \cdot 100 \%. \tag{19}$$

Precision is calculated as the number of true positives  $T_P$  divided by the total number of true positives and also false positives  $F_P$  and is calculated as follows:

$$\text{Precision} = \frac{T_P}{T_P + F_P} \cdot 100 \%. \tag{20}$$

In this case, the  $C_{EFF}$  of the MLP model equals 97.3%. Misclassifications are visible mainly for the very early stage of the fault—for  $N_{sh} = 1$ . The precision for this model is as high as 99.7%.

### 6.2.2. SVM

In order to select the SVM model most suitable for the PMSM stator winding fault classification task, different types of kernel functions are analyzed: linear, quadratic, cubic and Gaussian with different function widths. The accuracies of the SVM models for different kernel functions are presented in Table 2. The lowest accuracy of 96.0% is achieved by a linear SVM model, while the highest accuracy of 98.9% is achieved by an SVM model with a Gaussian kernel function of width 0.4.

**Table 2.** The SVM classifier accuracy for different kernel functions.

Kernel Function	Accuracy	$\sigma$ [-]
Linear	96.0%	
Quadratic	96.5%	-
Cubic	98.4%	
Gaussian	98.4%	0.1
	98.8%	0.2
	98.8%	0.3
	<b>98.9%</b>	<b>0.4</b>
	98.8%	0.5
	98.8%	0.6
	98.8%	0.7
	98.7%	0.8
	98.7%	0.9

The responses of the SVM-based PMSM stator winding classifier and actual stator winding conditions ( $N_{st}$ ) to the test vectors are shown in Figure 17. In this case, the classification effectiveness achieved is equal to 98.8%, while the precision to 100.0%. Compared to MLP, there are far fewer misclassifications for the undamaged winding and one shorted turn, which is a significant advantage.

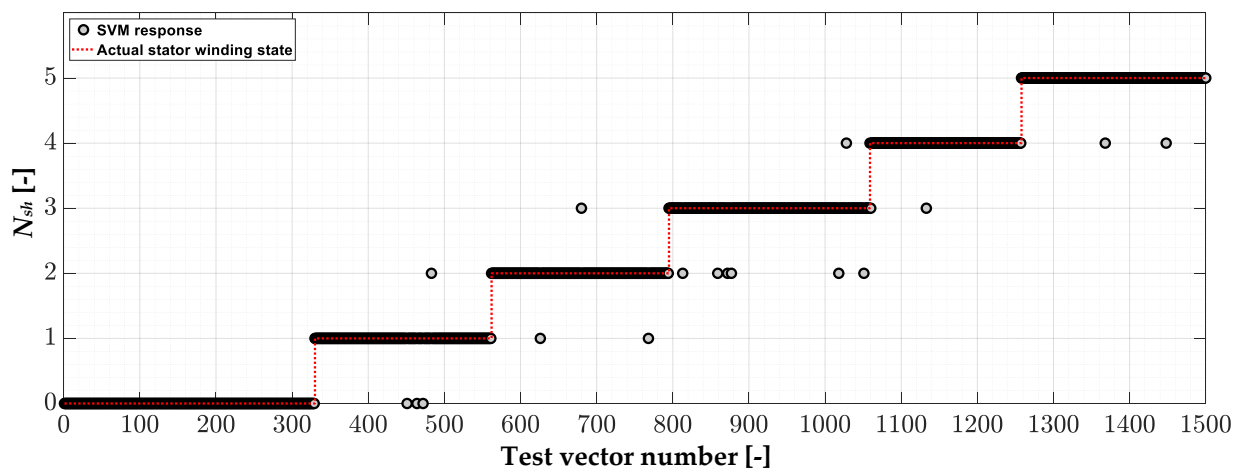


**Figure 17.** Responses of the SVM-based fault classifier model to the test vectors.

### 6.2.3. KNN

The hyperparameters of the KNN model are the  $K$  value and the distance metric. The accuracies of the KNN-based ITSC fault classifier model for different sets of parameters are shown in Table 3. Based on the analysis of the results, it can be concluded that the lowest accuracy over the entire range of  $K$  values studied is obtained by KNN with the correlation distance metric, while the highest accuracy equals 98.9% for  $K = 3$  and Euclidean distance. The responses of the KNN classifier to the test vectors are shown in Figure 18. The classification effectiveness achieved is the same as that for the SVM model—98.8%. The precision for this model is 100.0%.

### 6.2.4. On-Line Verification

In order to verify the operation of the ML-based fault classifier during the on-line operation of the drive system, an automatic condition monitoring system is developed. The block diagram of its concept is presented in Figure 19. Among its key elements is the acquisition of the data from measured phase current signals transferred to the DAQ card, using the DAQ Assistant block available in the LabVIEW environment. Those signals are

then passed to the MATLAB script structure available in LabVIEW. It calls the MATLAB software to execute scripts. In the MATLAB script developed,  $|i_s|$  is calculated according to Equation (3), and complex generalized Morse wavelet-based CWT is also performed (*MATLAB Wavelet Toolbox*, MATLAB version: R2020b). Then the input vector that contains the values of the selected components that we proved are the most sensitive to the stator winding fault is passed to the ML classifier model. The models analyzed in our research are trained using the *Statistics and Machine Learning Toolbox*. The developed and pre-trained model automatically infers the stator winding condition based on the input vector.

**Table 3.** The KNN classifier accuracy for different key parameters.

K [–]	Distance Metric		
	Euclidean	Minkowski	Correlation
1	98.6%	98.4%	74.4%
2	98.4%	98.4%	74.7%
3	<b>98.9%</b>	98.6%	77.4%
4	98.4%	98.4%	79.1%
5	98.5%	98.4%	79.5%
10	98.3%	98.2%	80.6%
15	98.2%	98.2%	80.2%
20	98.0%	98.0%	79.6%
25	97.9%	97.3%	79.2%
30	97.3%	97.3%	78.6%
35	96.5%	96.5%	78.1%
40	94.7%	94.5%	77.0%
45	92.4%	91.7%	76.3%
50	87.1%	86.2%	75.1%
75	82.9%	81.6%	71.3%
100	78.5%	77.5%	66.9%

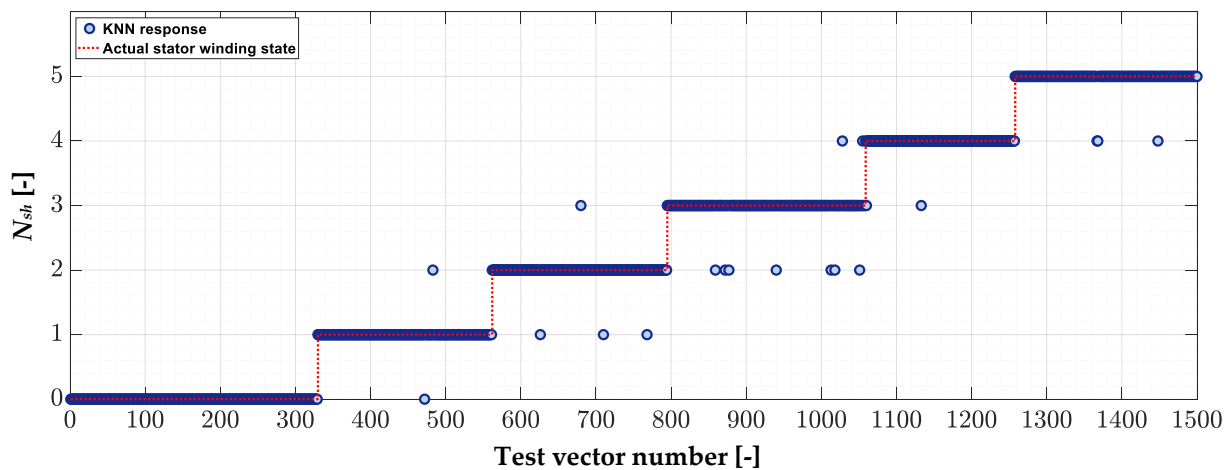


**Figure 18.** Responses of the KNN-based fault classifier model to the test vectors.

The actual stator winding conditions and responses of the MLP-based fault classifier for the on-line operation of the PMSM drive are shown in Figure 20. During this test, one to five turns in phase A are sequentially shorted for about 1–2 s for different load torque levels. The classification effectiveness of the MLP model for this test is equal to 96.1%. The responses of the SVM model for the same test case are shown in Figure 21. The results show that the classification effectiveness is lower than that for the MLP model and equals 95.8%. The last of the verified ML-based models is KNN. The result of the test of this classifier is presented in Figure 22. This model achieved the highest effectiveness, equaling 97.1%.

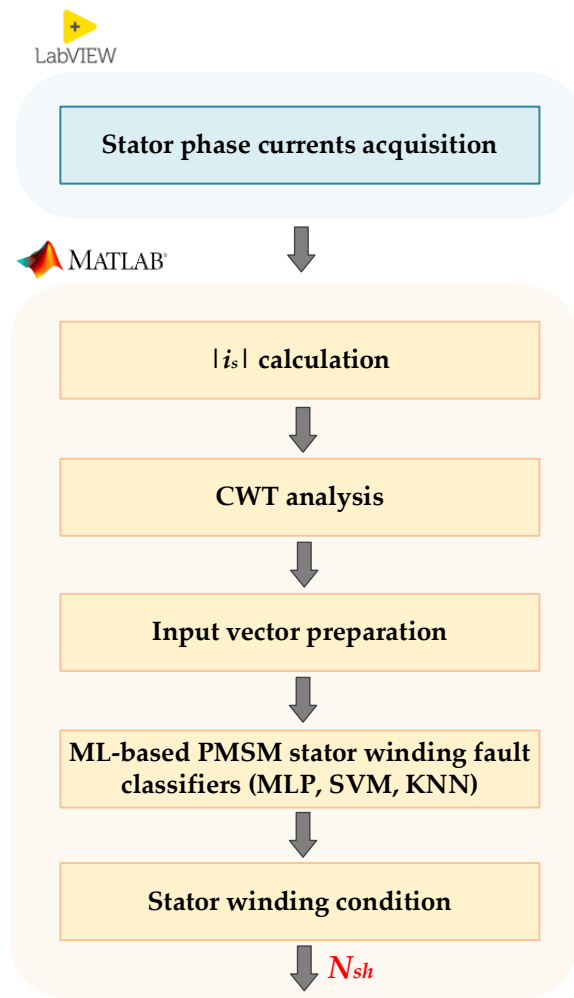


Figure 19. Block diagram of the proposed fault diagnosis method.

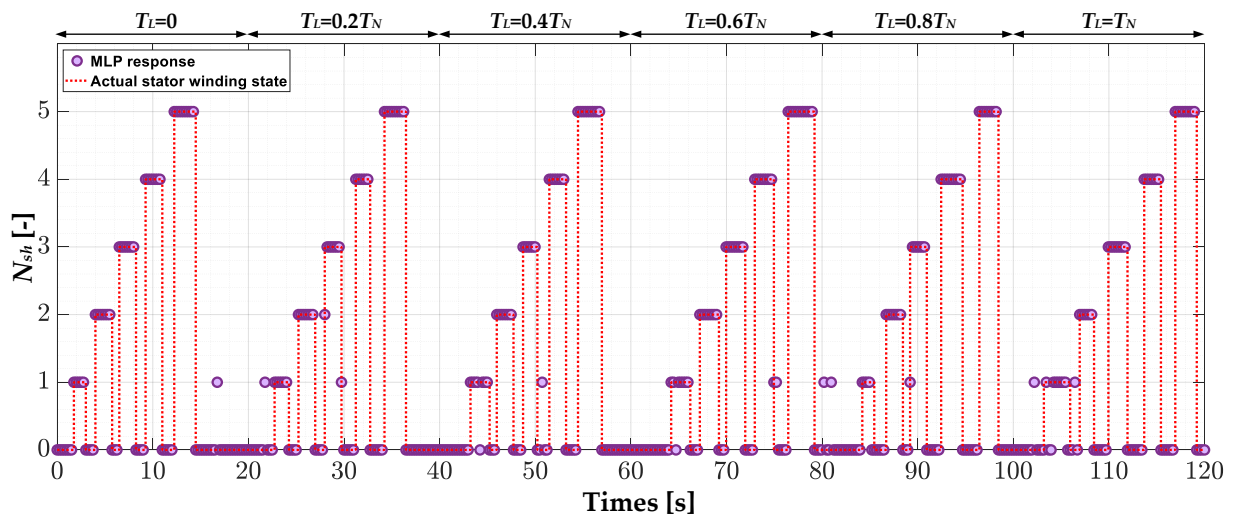


Figure 20. The actual states of the stator windings and MLP model responses of the fault classifier models for on-line operation of the PMSM drive.

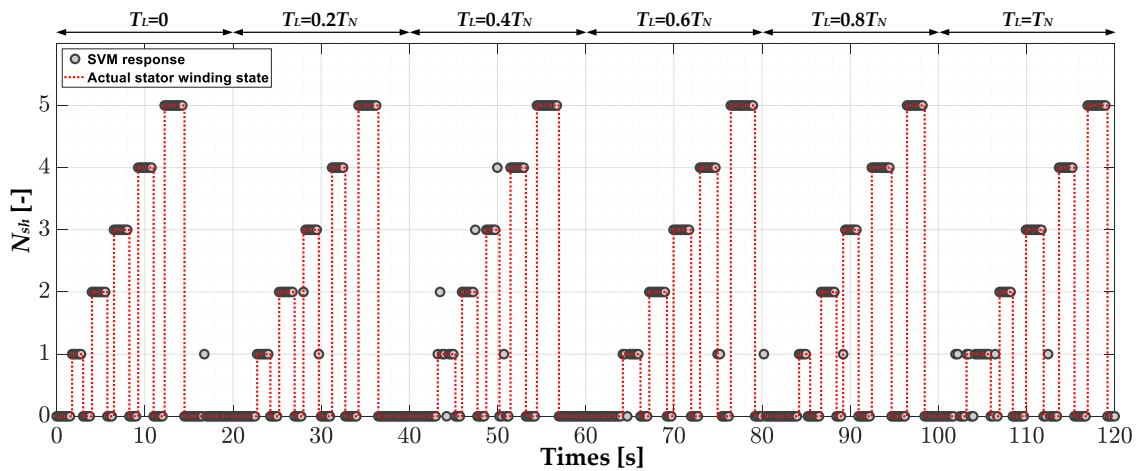


Figure 21. The actual states of the stator windings and SVM model responses of the fault classifier models for on-line operation of the PMSM drive.

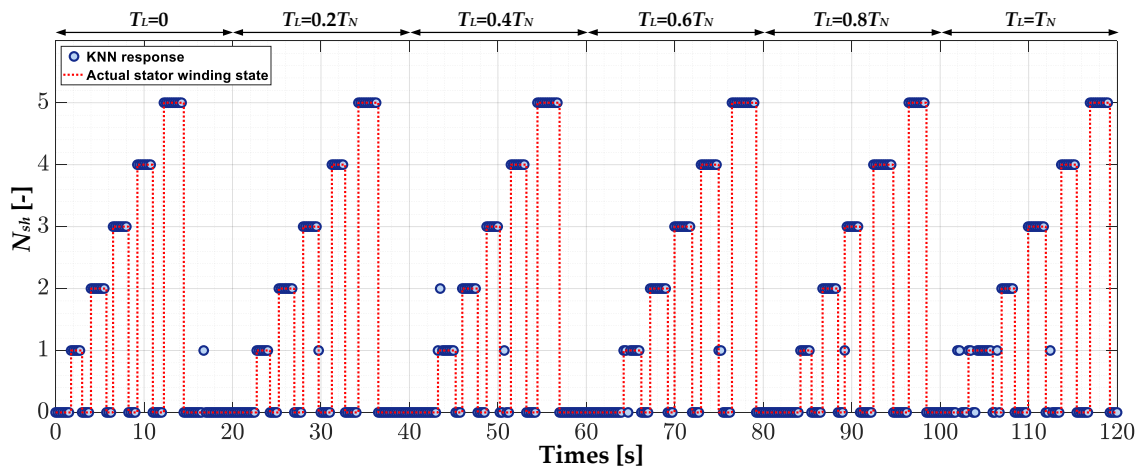


Figure 22. The actual states of the stator windings and KNN model responses of the fault classifier models for on-line operation of the PMSM drive.

Based on the results presented in Figures 20–22, it can be concluded that all the prepared models achieved high, similar effectiveness in classifying the condition of the PMSM stator winding. The comparison of the accuracy, classification effectiveness and precision of the analyzed ML-based classifiers is summarized in Table 4. Nevertheless, in the case of ITSCs, a short detection time is crucial. Therefore, the response times of the analyzed models are compared to finally evaluate these models. The comparison of response times for 10,000 trials is presented in Figure 23. Significantly shorter time ( $\approx 3$  times) compared to SVM and MLP is visible for the KNN model, which is a notable advantage.

Table 4. The comparison of the analyzed ML-based classifiers.

Metric	ML-Based Classifier		
	MLP	SVM	KNN
Model Accuracy [%]	98.1%	98.8%	98.8%
Off-line test	$C_{EFF}$ [%]	97.3%	98.8%
	Precision [%]	99.7%	100.0%
On-line test	$C_{EFF}$ [%]	96.1%	95.8%
	Precision [%]	95.7%	95.7%

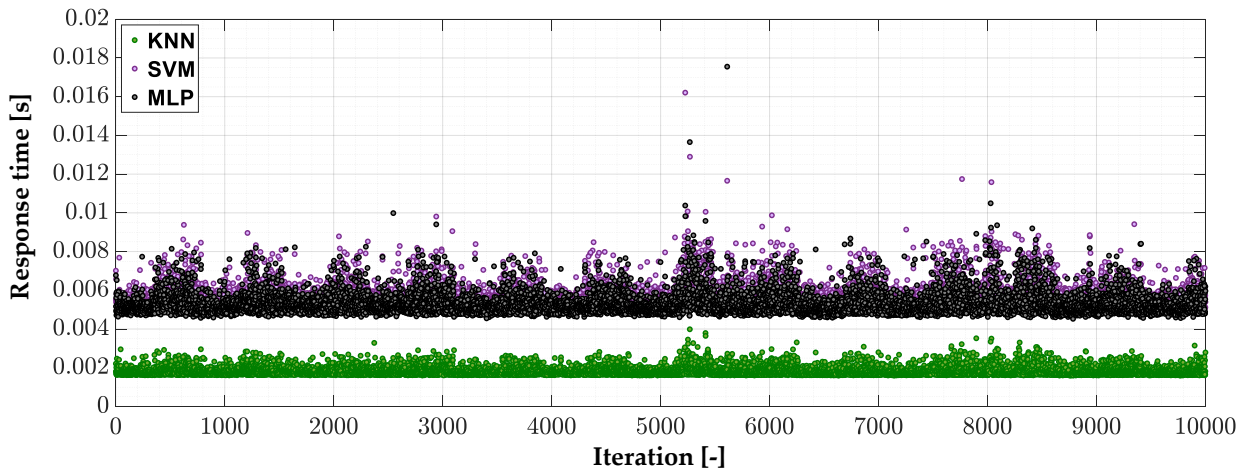


Figure 23. Comparison of the response time of the developed classifier models.

Nevertheless, in addition to the model’s response time, in order to realize one complete iteration of the developed fault diagnosis algorithms, the time consumed consists of the measurement time (data collection of the stator phase current signal) and computation time of the signal processing ( $|i_s|$  and its CWT calculation). The sum of these times represents the exact detection time. A comparison of the time consumed by the different diagnostic techniques is shown in Figure 24. The data collection time (stator phase current measurement time) is the same in each case and is equal to 0.25 s. It allows the collection of 2048 samples of the stator phase current. The stator phase current space vector module calculation and CWT analysis consume 13.6 ms on average. The average model response time for 10,000 trials equals 5.8 ms, 5.9 ms and 1.9 ms for the MLP, SVM and KNN models, respectively. Based on these results, it can be concluded that the shortest time (0.266 s) required to infer the PMSM winding conditions (detection time) is obtained using the KNN model.

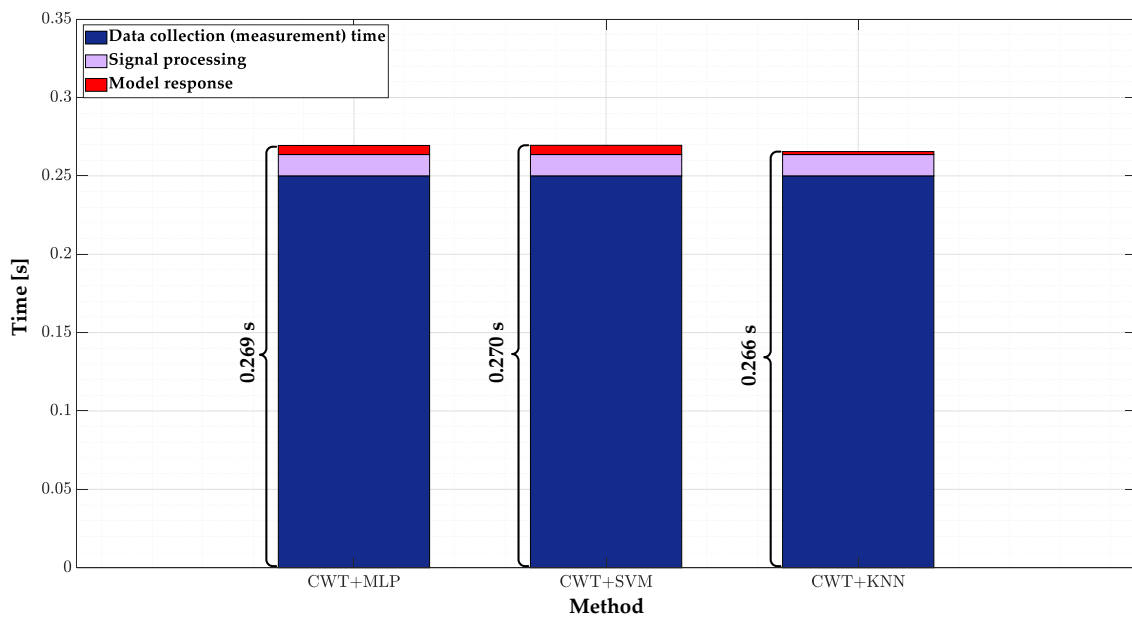


Figure 24. Comparison of the time consumed by different diagnosis techniques.

### 7. Conclusions

Experimental verification confirmed the feasibility of using CWT analysis of the stator phase current, its envelope and the space vector module signal to extract symptoms of

PMSM stator winding fault. Extraction of the symptoms most sensitive to stator winding damage—whose value increase is the greatest and visible even with one shorted turn—was obtained for CWT analysis of the stator current space vector module. For the current signal and its envelope, the increases in the values of the extracted CWT coefficients are less significant, but still noticeable, especially from two shorted turns in the winding.

Thanks to the careful selection of input vector elements, the developed fault classifiers based on the MLP, SVM and KNN models have achieved very high efficiency in both off-line and on-line tests. The best classification effectiveness and precision and the shortest detection time were obtained for the KNN model. However, both MLP and SVM can be successfully applied to automate the process of monitoring the condition of PMSM stator windings. It has also been proven that in order to maximize the effectiveness of ML-based fault detectors, it is necessary to carefully select their key parameters.

Given that low-cost solutions are sought in industrial applications, and the KNN algorithm is an algorithm that is simple for embedded implementation and requires low computational power, future research will focus on developing a diagnostic system that is based on it and is cost-optimized while maintaining high effectiveness in the automatic condition monitoring process.

**Author Contributions:** All of the authors contributed equally to the concept of the paper and proposed the methodology; investigation and formal analyses, P.P. and M.W.; software and data curation, P.P.; measurements, P.P. and M.W.; proposed the paper organization, P.P. and M.W.; validated the obtained results, M.W. All authors have read and agreed to the published version of the manuscript.

**Funding:** This research received no external funding.

**Data Availability Statement:** Not applicable.

**Conflicts of Interest:** The authors declare no conflict of interest.

## Appendix A

**Table A1.** Rated parameters of the tested PMSM.

Name of the Parameter	Symbol	Units	
Power	$P_N$	2500	W
Torque	$T_N$	16	Nm
Speed	$n_N$	1500	r/min
Stator phase voltage	$U_{sN}$	325	V
Stator current	$I_{sN}$	6.6	A
Frequency	$f_{sN}$	100	Hz
Number of pole pairs	$p_p$	4	-
Number of stator turns	$N_{st}$	$2 \times 125$	-

## References

1. Attaianese, C.; D'Arpino, M.; Monaco, M.; Di Noia, L.P. Model-Based Detection and Estimation of DC Offset of Phase Current Sensors for Field Oriented PMSM Drives. *IEEE Trans. Ind. Electron.* **2023**, *70*, 6316–6325. [\[CrossRef\]](#)
2. Yan, H.; Wang, W.; Xu, Y.; Zou, J. Position Sensorless Control for PMSM Drives With Single Current Sensor. *IEEE Trans. Ind. Electron.* **2023**, *70*, 178–188. [\[CrossRef\]](#)
3. Pietrzak, P.; Wolkiewicz, M. Machine Learning-Based Stator Current Data-Driven PMSM Stator Winding Fault Diagnosis. *Sensors* **2022**, *22*, 9668. [\[CrossRef\]](#) [\[PubMed\]](#)
4. Ewert, P.; Orłowska-Kowalska, T.; Jankowska, K. Effectiveness Analysis of PMSM Motor Rolling Bearing Fault Detectors Based on Vibration Analysis and Shallow Neural Networks. *Energies* **2021**, *14*, 712. [\[CrossRef\]](#)
5. Pietrzak, P.; Wolkiewicz, M. Demagnetization Fault Diagnosis of Permanent Magnet Synchronous Motors Based on Stator Current Signal Processing and Machine Learning Algorithms. *Sensors* **2023**, *23*, 1757. [\[CrossRef\]](#) [\[PubMed\]](#)
6. Jankowska, K.; Dybkowski, M. A Current Sensor Fault Tolerant Control Strategy for PMSM Drive Systems Based on Cri Markers. *Energies* **2021**, *14*, 3443. [\[CrossRef\]](#)
7. Orłowska-Kowalska, T.; Wolkiewicz, M.; Pietrzak, P.; Skowron, M.; Ewert, P.; Tarchala, G.; Krzysztofiak, M.; Kowalski, C.T. Fault Diagnosis and Fault-Tolerant Control of PMSM Drives—State of the Art and Future Challenges. *IEEE Access* **2022**, *10*, 59979–60024. [\[CrossRef\]](#)

8. Chen, Y.; Liang, S.; Li, W.; Liang, H.; Wang, C. Faults and Diagnosis Methods of Permanent Magnet Synchronous Motors: A Review. *Appl. Sci.* **2019**, *9*, 2116. [[CrossRef](#)]
9. He, J.; Somogyi, C.; Strandt, A.; Demerdash, N.A.O. Diagnosis of Stator Winding Short-Circuit Faults in an Interior Permanent Magnet Synchronous Machine. In Proceedings of the 2014 IEEE Energy Conversion Congress and Exposition (ECCE), Pittsburgh, PA, USA, 14–18 September 2014; pp. 3125–3130.
10. Drif, M.; Cardoso, A.J.M. Stator Fault Diagnostics in Squirrel Cage Three-Phase Induction Motor Drives Using the Instantaneous Active and Reactive Power Signature Analyses. *IEEE Trans. Ind. Inf.* **2014**, *10*, 1348–1360. [[CrossRef](#)]
11. Pietrzak, P.; Wolkiewicz, M. On-Line Detection and Classification of PMSM Stator Winding Faults Based on Stator Current Symmetrical Components Analysis and the KNN Algorithm. *Electronics* **2021**, *10*, 1786. [[CrossRef](#)]
12. Haddad, R.Z.; Strangas, E.G. Fault Detection and Classification in Permanent Magnet Synchronous Machines Using Fast Fourier Transform and Linear Discriminant Analysis. In Proceedings of the 2013 9th IEEE International Symposium on Diagnostics for Electric Machines, Power Electronics and Drives (SDEMPED), Valencia, Spain, 27–30 August 2013; pp. 99–104.
13. Ahn, G.; Lee, J.; Park, C.H.; Youn, M.; Youn, B.D. Inter-Turn Short Circuit Fault Detection in Permanent Magnet Synchronous Motors Based on Reference Voltage. In Proceedings of the 2019 IEEE 12th International Symposium on Diagnostics for Electrical Machines, Power Electronics and Drives (SDEMPED), Valencia, Spain, 27–30 August 2019; pp. 245–250.
14. Fang, J.; Sun, Y.; Wang, Y.; Wei, B.; Hang, J. Improved ZSVC-based Fault Detection Technique for Incipient Stage Inter-turn Fault in PMSM. *IET Electr. Power Appl.* **2019**, *13*, 2015–2026. [[CrossRef](#)]
15. Laadjal, K.; Bento, F.; Henriques, K.; Marques Cardoso, A.J.; Sahrroui, M. A Novel Indicator-Based On-Line Diagnostics Technique of Inter-Turn Short-Circuit Faults in Synchronous Reluctance Machines. *IEEE J. Emerg. Sel. Top. Power Electron.* **2023**, *1*. [[CrossRef](#)]
16. Gurusamy, V.; Bostanci, E.; Li, C.; Qi, Y.; Akin, B. A Stray Magnetic Flux-Based Robust Diagnosis Method for Detection and Location of Interturn Short Circuit Fault in PMSM. *IEEE Trans. Instrum. Meas.* **2021**, *70*, 3500811. [[CrossRef](#)]
17. Skowron, M.; Wolkiewicz, M.; Orłowska-Kowalska, T.; Kowalski, C.T. Effectiveness of Selected Neural Network Structures Based on Axial Flux Analysis in Stator and Rotor Winding Incipient Fault Detection of Inverter-Fed Induction Motors. *Energies* **2019**, *12*, 2392. [[CrossRef](#)]
18. Sarikhani, A.; Mohammed, O.A. Inter-Turn Fault Detection in PM Synchronous Machines by Physics-Based Back Electromotive Force Estimation. *IEEE Trans. Ind. Electron.* **2013**, *60*, 3472–3484. [[CrossRef](#)]
19. Zhou, Y.; Kumar, A.; Parkash, C.; Vashishtha, G.; Tang, H.; Glowacz, A.; Dong, A.; Xiang, J. Development of Entropy Measure for Selecting Highly Sensitive WPT Band to Identify Defective Components of an Axial Piston Pump. *Appl. Acoust.* **2023**, *203*, 109225. [[CrossRef](#)]
20. Wolkiewicz, M.; Tarchala, G.; Orłowska-Kowalska, T.; Kowalski, C.T. Online Stator Interturn Short Circuits Monitoring in the DFOC Induction-Motor Drive. *IEEE Trans. Ind. Electron.* **2016**, *63*, 2517–2528. [[CrossRef](#)]
21. Krzysztofiak, M.; Skowron, M.; Orłowska-Kowalska, T. Analysis of the Impact of Stator Inter-Turn Short Circuits on PMSM Drive with Scalar and Vector Control. *Energies* **2020**, *14*, 153. [[CrossRef](#)]
22. Lee, J.; Moon, S.; Jeong, H.; Kim, S. Robust Diagnosis Method Based on Parameter Estimation for an Interturn Short-Circuit Fault in Multipole PMSM under High-Speed Operation. *Sensors* **2015**, *15*, 29452–29466. [[CrossRef](#)]
23. Pietrzak, P.; Wolkiewicz, M. Comparison of Selected Methods for the Stator Winding Condition Monitoring of a PMSM Using the Stator Phase Currents. *Energies* **2021**, *14*, 1630. [[CrossRef](#)]
24. Bhuiyan, E.A.; Akhand, M.M.A.; Das, S.K.; Ali, M.F.; Tasneem, Z.; Islam, M.R.; Saha, D.K.; Badal, F.R.; Ahamed, M.H.; Moyeen, S.I. A Survey on Fault Diagnosis and Fault Tolerant Methodologies for Permanent Magnet Synchronous Machines. *Int. J. Autom. Comput.* **2020**, *17*, 763–787. [[CrossRef](#)]
25. Haddad, R.Z.; Strangas, E.G. On the Accuracy of Fault Detection and Separation in Permanent Magnet Synchronous Machines Using MCSA/MVSA and LDA. *IEEE Trans. Energy Convers.* **2016**, *31*, 924–934. [[CrossRef](#)]
26. Cruz, S.M.A.; Cardoso, A.J.M. Stator Winding Fault Diagnosis in Three-Phase Synchronous and Asynchronous Motors, by the Extended Park's Vector Approach. *IEEE Trans. Ind. Appl.* **2001**, *37*, 1227–1233. [[CrossRef](#)]
27. Rosero, J.; Ortega, J.; Urresty, J.; Cardenas, J.; Romeral, L. Stator Short Circuits Detection in PMSM by Means of Higher Order Spectral Analysis (HOSA). In Proceedings of the 2009 Twenty-Fourth Annual IEEE Applied Power Electronics Conference and Exposition, Washington, DC, USA, 15–19 February 2009; pp. 964–969.
28. Pietrzak, P.; Wolkiewicz, M.; Orłowska-Kowalska, T. PMSM Stator Winding Fault Detection and Classification Based on Bispectrum Analysis and Convolutional Neural Network. *IEEE Trans. Ind. Electron.* **2022**, *70*, 5192–5202. [[CrossRef](#)]
29. Urresty, J.; Riba, J.; Romeral, L.; Rosero, J.; Serna, J. Stator Short Circuits Detection in PMSM by Means of Hilbert-Huang Transform and Energy Calculation. In Proceedings of the 2009 IEEE International Symposium on Diagnostics for Electric Machines, Power Electronics and Drives, Cargese, France, 31 August 2009; pp. 1–7.
30. Rosero, J.A.; Romeral, L.; Ortega, J.A.; Rosero, E. Short-Circuit Detection by Means of Empirical Mode Decomposition and Wigner–Ville Distribution for PMSM Running Under Dynamic Condition. *IEEE Trans. Ind. Electron.* **2009**, *56*, 4534–4547. [[CrossRef](#)]
31. Pietrzak, P.; Wolkiewicz, M. Stator Phase Current STFT Analysis for the PMSM Stator Winding Fault Diagnosis. In Proceedings of the 2022 International Symposium on Power Electronics, Electrical Drives, Automation and Motion (SPEEDAM), Sorrento, Italy, 22 June 2022; pp. 808–813.

32. Al Duhayyim, M.G.; Mohamed, H.S.; Alzahrani, J.; Alabdan, R.; Aziz, A.S.A.; Zamani, A.S.; Yaseen, I.; Alsaid, M.I. Sandpiper Optimization with a Deep Learning Enabled Fault Diagnosis Model for Complex Industrial Systems. *Electronics* **2022**, *11*, 4190. [[CrossRef](#)]
33. Zaman, S.M.K.; Marma, H.U.M.; Liang, X. Broken Rotor Bar Fault Diagnosis for Induction Motors Using Power Spectral Density and Complex Continuous Wavelet Transform Methods. In Proceedings of the 2019 IEEE Canadian Conference of Electrical and Computer Engineering (CCECE), Edmonton, AB, Canada, 5–8 May 2019; pp. 1–4.
34. Skowron, M.; Krzysztofciak, M.; Orłowska-Kowalska, T. Effectiveness of Neural Fault Detectors of Permanent Magnet Synchronous Motor Trained With Symptoms From Field-Circuit Modeling. *IEEE Access* **2022**, *10*, 104598–104611. [[CrossRef](#)]
35. Skowron, M.; Orłowska-Kowalska, T.; Kowalski, C.T. Diagnosis of Stator Winding and Permanent Magnet Faults of PMSM Drive Using Shallow Neural Networks. *Electronics* **2023**, *12*, 1068. [[CrossRef](#)]
36. Song, Q.; Wang, M.; Lai, W.; Zhao, S. On Bayesian Optimization-Based Residual CNN for Estimation of Inter-Turn Short Circuit Fault in PMSM. *IEEE Trans. Power Electron.* **2023**, *38*, 2456–2468. [[CrossRef](#)]
37. Skowron, M.; Orłowska-Kowalska, T.; Kowalski, C.T. Detection of Permanent Magnet Damage of PMSM Drive Based on Direct Analysis of the Stator Phase Currents Using Convolutional Neural Network. *IEEE Trans. Ind. Electron.* **2022**, *69*, 13665–13675. [[CrossRef](#)]
38. Zhou, Y.; Kumar, A.; Parkash, C.; Vashishtha, G.; Tang, H.; Xiang, J. A Novel Entropy-Based Sparsity Measure for Prognosis of Bearing Defects and Development of a Sparsogram to Select Sensitive Filtering Band of an Axial Piston Pump. *Measurement* **2022**, *203*, 111997. [[CrossRef](#)]
39. Skowron, M.; Kowalski, C.T. Permanent Magnet Synchronous Motor Fault Detection System Based on Transfer Learning Method. In Proceedings of the IECON 2022—48th Annual Conference of the IEEE Industrial Electronics Society, Brussels, Belgium, 17 October 2022; pp. 1–6.
40. Kaplan, H.; Tehrani, K.; Jamshidi, M. A Fault Diagnosis Design Based on Deep Learning Approach for Electric Vehicle Applications. *Energies* **2021**, *14*, 6599. [[CrossRef](#)]
41. Zhao, Y.-P.; Huang, G.; Hu, Q.-K.; Li, B. An Improved Weighted One Class Support Vector Machine for Turboshaft Engine Fault Detection. *Eng. Appl. Artif. Intell.* **2020**, *94*, 103796. [[CrossRef](#)]
42. Romeral, L.; Urresty, J.C.; Riba Ruiz, J.-R.; Garcia Espinosa, A. Modeling of Surface-Mounted Permanent Magnet Synchronous Motors With Stator Winding Interturn Faults. *IEEE Trans. Ind. Electron.* **2011**, *58*, 1576–1585. [[CrossRef](#)]
43. Zhang, J.; Tounzi, A.; Benabou, A.; le Menach, Y. Detection of Magnetization Loss in a PMSM with Hilbert Huang Transform Applied to Non-Invasive Search Coil Voltage. *Math Comput. Simul.* **2021**, *184*, 184–195. [[CrossRef](#)]
44. Attestog, S.; van Khang, H.; Robbersmyr, K.G. Field Reconstruction for Modeling Multiple Faults in Permanent Magnet Synchronous Motors in Transient States. *IEEE Access* **2021**, *9*, 127131–127140. [[CrossRef](#)]
45. Cohen, L. Time-Frequency Distributions—a Review. *Proc. IEEE* **1989**, *77*, 941–981. [[CrossRef](#)]
46. Shao, S.; Yan, R.; Lu, Y.; Wang, P.; Gao, R.X. DCNN-Based Multi-Signal Induction Motor Fault Diagnosis. *IEEE Trans. Instrum. Meas.* **2020**, *69*, 2658–2669. [[CrossRef](#)]
47. Diao, N.; Wang, Z.; Ma, H.; Yang, W. Fault Diagnosis of Rolling Bearing Under Variable Working Conditions Based on CWT and T-ResNet. *J. Vib. Eng. Technol.* **2022**, 1–11. [[CrossRef](#)]
48. Konar, P.; Saha, M.; Sil, J.; Chattopadhyay, P. Fault Diagnosis of Induction Motor Using CWT and Rough-Set Theory. In Proceedings of the 2013 IEEE Symposium on Computational Intelligence in Control and Automation (CICA), Singapore, 16–19 April 2013; pp. 17–23.
49. Ho, K.C.; Prokopiw, W.; Chan, Y.T. Modulation Identification of Digital Signals by the Wavelet Transform. *IEE Proc.-Radar. Sonar. Navig.* **2000**, *147*, 169. [[CrossRef](#)]
50. Daubechies, I. Orthonormal Bases of Compactly Supported Wavelets. *Commun Pure. Appl. Math.* **1988**, *41*, 909–996. [[CrossRef](#)]
51. Teolis, A. *Computational Signal Processing with Wavelets*; Birkhäuser Boston: Boston, MA, USA, 1998; ISBN 978-1-4612-8672-1.
52. Lilly, J.M.; Olhede, S.C. Higher-Order Properties of Analytic Wavelets. *IEEE Trans. Signal Process.* **2009**, *57*, 146–160. [[CrossRef](#)]
53. Lilly, J.M.; Olhede, S.C. On the Analytic Wavelet Transform. *IEEE Trans. Inf. Theory* **2010**, *56*, 4135–4156. [[CrossRef](#)]
54. Lilly, J.M.; Olhede, S.C. Generalized Morse Wavelets as a Superfamily of Analytic Wavelets. *IEEE Trans. Signal Process.* **2012**, *60*, 6036–6041. [[CrossRef](#)]
55. Malarczyk, M.; Zychlewicz, M.; Stanislawski, R.; Kaminski, M. Low-Cost Implementation of an Adaptive Neural Network Controller for a Drive with an Elastic Shaft. *Signals* **2023**, *4*, 56–72. [[CrossRef](#)]
56. García-Cuesta, E.; Galván, I.M.; de Castro, A.J. Multilayer Perceptron as Inverse Model in a Ground-Based Remote Sensing Temperature Retrieval Problem. *Eng. Appl. Artif. Intell.* **2008**, *21*, 26–34. [[CrossRef](#)]
57. Shekofteh, Y.; Almasganj, F.; Daliri, A. MLP-Based Isolated Phoneme Classification Using Likelihood Features Extracted from Reconstructed Phase Space. *Eng. Appl. Artif. Intell.* **2015**, *44*, 1–9. [[CrossRef](#)]
58. Kaminski, M.; Orłowska-Kowalska, T. Adaptive Neural Speed Controllers Applied for a Drive System with an Elastic Mechanical Coupling—A Comparative Study. *Eng. Appl. Artif. Intell.* **2015**, *45*, 152–167. [[CrossRef](#)]
59. Chiddarwar, S.S.; Ramesh Babu, N. Comparison of RBF and MLP Neural Networks to Solve Inverse Kinematic Problem for 6R Serial Robot by a Fusion Approach. *Eng. Appl. Artif. Intell.* **2010**, *23*, 1083–1092. [[CrossRef](#)]

60. Kisi, Ö. Multi-Layer Perceptrons with Levenberg-Marquardt Training Algorithm for Suspended Sediment Concentration Prediction and Estimation/Prévision et Estimation de La Concentration En Matières En Suspension Avec Des Perceptrons Multi-Couches et l'algorithme d'apprentissage de Levenberg-Marquardt. *Hydrol. Sci. J.* **2004**, *49*, 1025–1040. [[CrossRef](#)]
61. Vapnik, V.N. *The Nature of Statistical Learning Theory*; Springer: New York, NY, USA, 2000; ISBN 978-1-4419-3160-3.
62. Zhou, J.; Qiu, Y.; Zhu, S.; Armaghani, D.J.; Li, C.; Nguyen, H.; Yagiz, S. Optimization of Support Vector Machine through the Use of Metaheuristic Algorithms in Forecasting TBM Advance Rate. *Eng. Appl. Artif. Intell.* **2021**, *97*, 104015. [[CrossRef](#)]
63. Widodo, A.; Yang, B.-S. Support Vector Machine in Machine Condition Monitoring and Fault Diagnosis. *Mech. Syst. Signal Process* **2007**, *21*, 2560–2574. [[CrossRef](#)]
64. Namdari, M.; Jazayeri-Rad, H. Incipient Fault Diagnosis Using Support Vector Machines Based on Monitoring Continuous Decision Functions. *Eng. Appl. Artif. Intell.* **2014**, *28*, 22–35. [[CrossRef](#)]
65. Ma, C.; Chi, Y. KNN Normalized Optimization and Platform Tuning Based on Hadoop. *IEEE Access* **2022**, *10*, 81406–81433. [[CrossRef](#)]

**Disclaimer/Publisher's Note:** The statements, opinions and data contained in all publications are solely those of the individual author(s) and contributor(s) and not of MDPI and/or the editor(s). MDPI and/or the editor(s) disclaim responsibility for any injury to people or property resulting from any ideas, methods, instructions or products referred to in the content.